Title: Variscan post-collisional cooling and uplift of the Tatra Mountains crystalline block constrained by integrated zircon, apatite and titanite LA-(MC)-ICP-MS U-Pb dating and rare earth element analyses

Author: Aleksandra Gawęda, Krzysztof Szopa, David Chew, Gary J. O'Sullivan, Jolanta Burda, Urs Klötzli, Jan Golonka

Citation style Gawęda Aleksandra, Szopa Krzysztof, Chew David, O'Sullivan Gary J., Burda Jolanta, Klötzli Urs, Golonka Jan. (2018). Variscan post-collisional cooling and uplift of the Tatra Mountains crystalline block constrained by integrated zircon, apatite and titanite LA-(MC)-ICP-MS U-Pb dating and rare earth element analyses. "Chemical Geology" Vol. 484 (2018), s. 191-209. doi: 10.1016/j.chemgeo.2018.03.012

Chemical Geology 484 (2018) 191–209

Contents lists available at ScienceDirect

Chemical Geology

journal homepage: www.elsevier.com/locate/chemgeo

Invited research article

Variscan post-collisional cooling and uplift of the Tatra Mountains crystalline block constrained by integrated zircon, apatite and titanite LA-(MC)-ICP-MS U-Pb dating and rare earth element analyses

Aleksandra Gawęda[a,*], Krzysztof Szopa[a], David Chew[b], Gary J. O'Sullivan[b], Jolanta Burda[a], Urs Klötzli[c], Jan Golonka[d]

[a] Faculty of Earth Sciences, University of Silesia in Katowice, Będzińska st. 60, 41-200 Sosnowiec, Poland
[b] Department of Geology, School of Natural Sciences, Trinity College Dublin, Dublin 2, Ireland
[c] Department of Lithospheric Research, University of Vienna, Althanstrasse 14, 1090 Vienna, Austria
[d] Faculty of Geology, Geophysics and Environmental Protection, AGH University of Science and Technology, Al. Mickiewicza 30, 30-059 Kraków, Poland

ARTICLE INFO

Keywords:
Tatra Mountains
Amphibolite
Apatite
Titanite
U-Pb dating
REE patterns

ABSTRACT

LA-ICP-MS U-Pb dating of apatite, titanite and zircon from the metamorphic cover of the Western Tatra granite was undertaken to constrain the timing of metamorphic events related to the final stages of Variscan orogenesis and subsequent post-orogenic exhumation. Zircon was found only in one sample from the northern metamorphic envelope. U-Pb ages from the outermost rims of zircons define a concordia age of 346 ± 6 Ma, while the inner rims yield a concordia age of 385 ± 8 Ma. Apatite from three samples from the northern metamorphic envelope yield U-Pb ages of 351.8 ± 4.4 Ma, 346.7 ± 5.9 Ma and 342.6 ± 7.1 Ma. Titanite from an amphibolite from the southern metamorphic envelope yields a U-Pb age of 345.3 ± 4.5 Ma. The age of c. 345 Ma is interpreted to represent the climax of metamorphism and the onset of simultaneous exhumation of the entire Tatra Mountains massif, and is recorded mainly in the northern part of the metamorphic cover.

In the southern metamorphic envelope, distinct populations of apatite can be recognized within individual samples based on their rare earth element (REE) and actinide contents. One population of apatite (Ap1) yields a relatively imprecise U-Pb age of 340 ± 31 Ma. This population comprises apatite grains with very similar trace element compositions to apatite in the northern amphibolite samples, which suggests they crystallized under similar metamorphic conditions to their northern counterparts. A second apatite population (Ap2) yields an age of c. 328 ± 22 Ma, which is interpreted as neocrystalline apatite that formed during a late-Variscan (hydrothermal?) process involving (P, F, Ca, REE)-rich fluid migration. The youngest generation of apatite (Ap3) yields a U-Pb age of 260 ± 8 Ma and may have resulted from thermal resetting associated with the regional emplacement of Permian A-type granites. The proposed tectonic model assumes that rapid uplift (and cooling) of the Tatra block initiated at ca. 345 Ma, contemporaneous with anatexis. Subsequent fluid migration, possibly facilitated by extension related to the opening of Paleo-Tethys, affected only the southern part of the Tatra block.

1. Introduction

Understanding the timescales of cooling and exhumation of basement terranes is one of the key problems in geology, and in particular the exhumation rates of the deep crust are the subject of active debate (e.g. Corsini et al., 2010 and references therein). Equally, recognizing exhumed deep crust is important in geodynamics because it yields constraints on the magnitudes and rates involved in the transfer of mass and heat during orogeny (e.g. Teyssier, 2011 and references therein). Accessory minerals such as zircon, titanite and apatite can preserve U-Pb isotopic age information and are commonly used as probes for the evolution of the Earth's crust in exhumation studies. Because of its low diffusivity for Pb, the U-Pb zircon system is a robust and widely-used geochronometer (Lee et al., 1997) which can be used to date high-temperature metamorphic events (e.g. Roberts and Finger, 1997; Rubatto, 2002, 2017), with a closure temperature of at least 900 °C (Lee et al., 1997). Titanite typically exhibits relatively high U, Th and Pb contents and is commonly used to date magmatic crystallization in igneous rocks, while in metamorphic rocks the U-Pb titanite system can be used to date moderate- to high- temperature thermal events (Möller

* Corresponding author.
E-mail address: aleksandra.gaweda@us.edu.pl (A. Gawęda).

https://doi.org/10.1016/j.chemgeo.2018.03.012
Received 27 April 2017; Received in revised form 25 January 2018; Accepted 7 March 2018
Available online 10 March 2018
0009-2541/

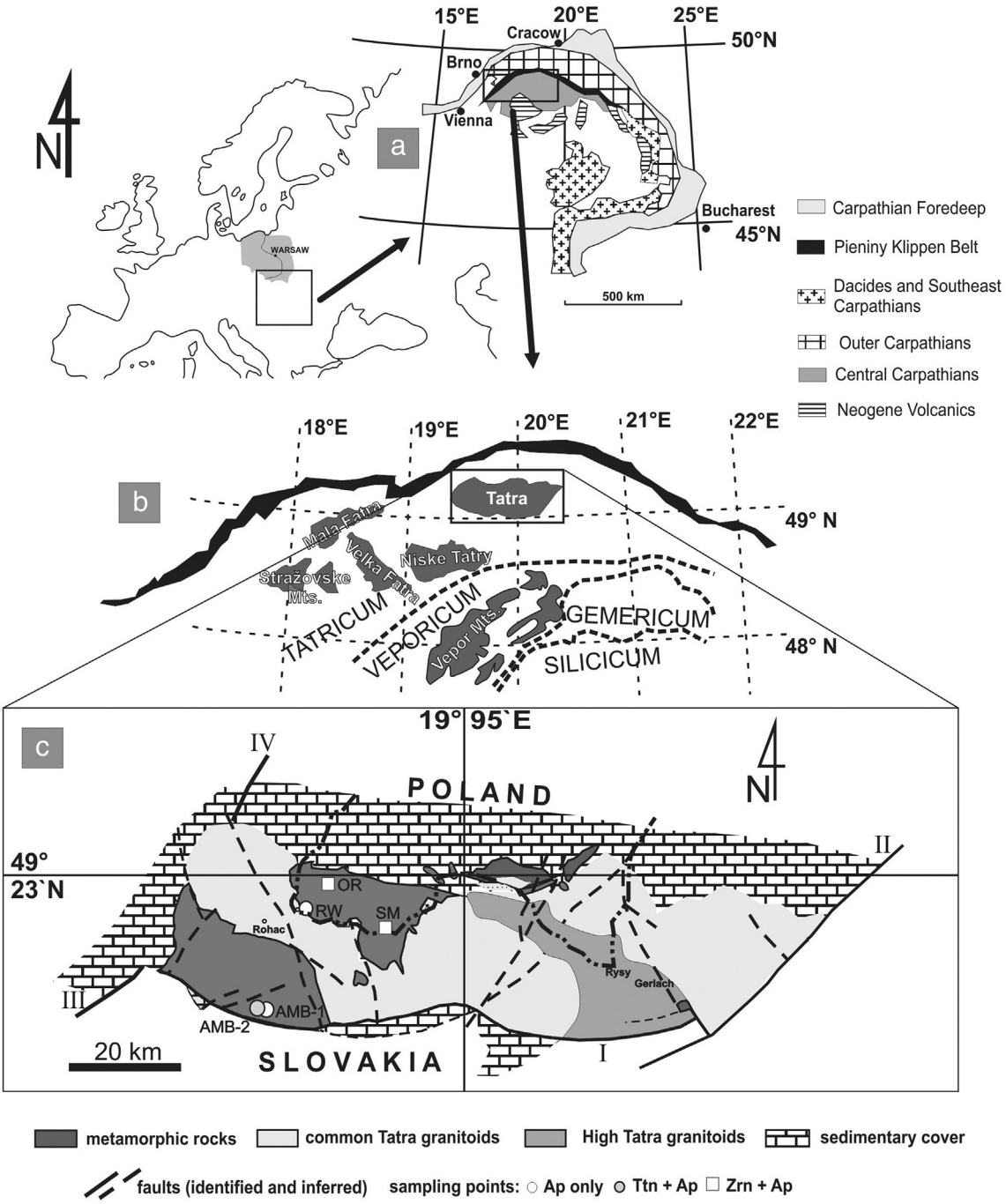

Fig. 1. (A) Simplified geological map of the Carpathian Chain showing the location of the Central Western Carpathians. (B) Map showing the location of the Variscan crystalline basement cores in the Central Western Carpathians including the Tatra Mountains. (C) Schematic geological map of the Tatra Mountains with the location of samples used for U-Pb dating. Data sources are Kohut and Janak, 1994; Petrik et al., 1994; Gawęda et al., 2016a and Piotrowska et al., 2014). Fault key: I – Sub-Tatric Fault, II – Ružbachy Fault, III – Choč Fault, IV – Krowiarki Fault.

et al., 2000; Buick et al., 2001; Schmitz and Bowring, 2001). The reported closure temperature variations are from 450°–500 °C to > 825 °C (Kohn, 2017 and references therein). The closure temperature window of the U-Pb system in apatite is lower (350–550 °C, Schoene and Bowring, 2007) and hence apatite U-Pb ages yield cooling history information for crystalline terranes (Chew and Spikings, 2015; Chew et al., 2011). Combining U-Pb age information from these three accessory phases thus yields valuable constraints on the medium- to high-temperature cooling (and hence exhumation) histories of crystalline massifs.

This study employs zircon, titanite and apatite laser ablation-inductively coupled plasma-mass spectrometry (LA-ICP-MS) U-Pb dating to constrain the timing of metamorphic events related to the final stages of orogenesis and subsequent post-orogenic uplift, using the Variscan Tatra massif in the Carpathians as a case study.

2. Geological setting and sampling

The Tatra Mountains block is one of several Variscan crystalline basement massifs within the Alpine belt of the Carpathians (Fig. 1a,b). The crystalline core of the Tatra Mountains comprises Variscan granitoid intrusions and its metamorphic envelope (Fig. 1c; Kohut and

Janak, 1994), and is partly covered by Mesozoic sediments which are incorporated within nappes associated with the Alpine orogenesis.

Polygenetic granitoid plutonism was formed by repeated magma injections from c. 370 to c. 340 Ma based on LA-ICP-MS U-Pb zircon dating (Gawęda et al., 2016a and references therein), with relatively rapid cooling at c. 340 Ma constrained by LA-ICP-MS U-Pb apatite dating (Gawęda et al., 2014). The metamorphic envelope to the polygenetic granitoid intrusions is exposed in the western part of the massif on both sides of the granitoid pluton, and underwent two stages of migmatization at c. 365 Ma and at c. 359 Ma (Burda and Gawęda, 2009; Fig. 1b). The metamorphic complex is composed of metapelitic-metapsammitic rocks (paragneisses and mica schists), intercalated with amphibolites, with three groups of amphibolites (Gawęda et al., 2000). Two amphibolite units have been dated by U-Pb zircon geochronology and likely represent two distinct oceanic domains that formed at c. 560 and c. 500 Ma (Gawęda et al., 2016b; Gawęda et al., 2017). A third amphibolite unit is garnet-bearing (Gawęda et al., 2000) and likely represents retrograde eclogites (Burda et al., 2015). Based on its trace element geochemistry and Sr-Nd isotope compositions, the protolith of the c. 560 Ma amphibolites was interpreted as MORB-type basalt (Gawęda et al., 2017), while the c. 500 Ma amphibolites likely represent tholeiitic basalts that intruded a basin floored by attenuated continental crust, as they exhibit varying degrees of lower crustal contamination (Gawęda et al., 2000; Gawęda et al., 2016b).

The emplacement of the Variscan plutons was associated with top-to-the-SE shear which mirrors the deformation history of the metamorphic envelope, suggesting these tabular plutons were emplaced *syn*-tectonically (Kohut and Janak, 1994; Gawęda and Szopa, 2011). Crystalline nappes within the metamorphic envelope are comprised of different lithologies and metamorphic grade (e.g. Gawęda et al., 2000; Gawęda and Burda, 2004; Burda and Gawęda, 2009). The nappes are bounded by local ductile and brittle-ductile shear zones, dated by the K-Ar method on syn-tectonic muscovite crystals at c. 343–298 Ma (Deditius, 2004). The formation of these nappe piles is linked to the closure of the Rheic Ocean and associated accretionary prism formation and is modified by subsequent post-orogenic uplift and associated granitoid magmatism (Gawęda et al., 2014; Moussallam et al., 2012).

The present-day disposition of units within the Tatra Mountains block is strongly influenced by Alpine orogenesis associated with the formation of the Western Carpathians Fold Belt. The Tatra Mountains block is bounded by faults (Fig. 1c), with the southern border of the block defined by the Sub-Tatric Fault (Fig. 1c). This fault allowed both exhumation of the Tatra block between 22 and 14 Ma (Śmigielski et al., 2016), and rotation of the entire Tatra block to the north by c. 30° (Grabowski and Gawęda, 1999). Regional seismic surveys show that the Tatra Block continues below the surface as far as the Pieniny Klippen Belt (Fig. 1b) under the Paleogene rocks of the Central Carpathian (Golonka et al., 2016).

For this study, two migmatized and two massive amphibolites were sampled. One sample of biotite paragneiss close to the contact with the common Tatra granite (sensu Kohut and Janak, 1994) was also collected. Two amphibolite samples (SM and OR) and one paragneiss (RW), weighting c. 10 kg each, were taken from the northern part of the Western Tatra Mountains metamorphic complex, while the two other amphibolite samples (AMB-1 and AMB-2) come from the southern part of the metamorphic envelope (Fig. 1c).

3. Analytical techniques

Fig. 1

3.1. Microscopy

Petrographic analyses of thin sections were undertaken at the Faculty of Earth Sciences in the University of Silesia, Poland using an Olympus BX-51 microscope to constrain textural and microstructural relationships and to determine the modal abundance and crystallization history of accessory apatite, titanite and zircon. These petrographical observations were used to select representative samples for subsequent electron probe micro-analysis, whole-rock geochemical analyses and U-Pb dating of zircon, apatite and titanite.

3.2. Electron probe micro-analyses (EPMA)

Microprobe analyses of the main rock-forming and accessory minerals were carried out at the Inter-Institutional Laboratory of Microanalyses of Minerals and Synthetic Substances, Warsaw, using a CAMECA SX-100 electron microprobe. The analytical conditions consisted of an accelerating voltage of 15 kV (or 50 kV for REE-bearing epidote), a beam current of 20 nA, counting times of 4 s per peak and background and a beam diameter of 1–5 μm. Reference materials, analytical lines, diffracting crystals, mean detection limits (in wt%) and uncertainties were as follows: rutile – Ti (Kα, PET, 0.03, 0.05), diopside – Mg (Kα, TAP, 0.02, 0.11), Si – (Kα, TAP, 0.02, 0.21), Ca – (Kα, PET, 0.03, 0.16), orthoclase – Al (Kα, TAP, 0.02, 0.08), and K (Kα, PET, 0.03, 0.02), albite – Na (Kα, TAP, 0.01, 0.08), hematite – Fe (Kα, LIF, 0.09, 0.47), rodonite – Mn (Kα, LIF, 0.03, 0.10), phlogophite – F (Kα, TAP, 0.04, 0.32), tugtupite – Cl (Kα, PET, 0.02, 0.04), Cr_2O_3 – Cr (Kα, PET, 0.04, 0.01), ZirconED2 – Zr (Lα, PET, 0.01, 0.01), Nb_2O_3-MAC – Nb (Lα, PET, 0.09, 0.01), V_2O_5 – V (Kα, LIF, 0.02, 0.01), YPO_4 – Y (Lα, TAP, 0.05, 0.05), La glass – La (Lα, LPET, 0.05, 0.03), CeP_5O_{14} – Ce (Lα, LPET, 0.09, 0.02), Pr-glass – Pr (Lβ, LIF, 0.04, 0.01), $NdGaO_3$ – Nd (Lβ, LIF, 0.31, 0.24), $GdPO_4$ – Gd (Lα, LIF, 0.34, 0.10), ThO_2 – Th (Mα, LPET, 0.09, 0.09), UO_2 – U (Mα, LPET, 0.16, 0.13).

3.3. Whole-rock analyses

Whole-rock analyses were undertaken by X-Ray fluorescence (XRF) for major and large ion lithophile trace Elements (LILE) and by fusion and ICP-MS for high field strength elements (HFSE) and rare earth elements (REE) in the ACME Analytical Laboratories (Canada). Preparation involved lithium borate fusion and dilute digestions for XRF and lithium borate decomposition or aqua regia digestion for ICP-MS. LOI was determined at 1000 °C. Uncertainties for most of major elements are 0.01%, except for SiO_2 which is 0.1% (Supplementary Table 1).

3.4. Mineral separation

Apatite, titanite and zircon crystals were separated using standard techniques (crushing, hydro-fracturing, washing, Wilfley shaking table, Frantz magnetic separator and hand picking). Mineral separation was carried out at the Institute of Geological Sciences at the Polish Academy of Sciences, Kraków, Poland. The crystals were then cast in 25 mm diameter epoxy resin mounts, ground and polished to half-thickness to expose the grain interiors. Internal mineral textures were then characterised by back-scattered electron (BSE) and cathodoluminescence (CL) imaging, using a FET Philips 30 scanning electron microscope with a 15 kV accelerating voltage and a beam current of 1 nA at the Faculty of Earth Sciences, University of Silesia, Sosnowiec, Poland.

3.5. Zircon U-Pb LA-MC-ICP-MS dating

The LA-MC-ICP-MS analytical work on zircon was performed at the joint ICP-MS laboratory of the Department of Earth Sciences, Karl-Franzens-University Graz and the Institute of Applied Geosciences, Graz Technical University, Austria.

Analytical procedures were identical to the methodology outlined in Klötzli et al. (2009). Zircon $^{206}Pb/^{238}U$ and $^{207}Pb/^{206}Pb$ ratios were determined using a 193 nm Ar-F excimer laser (ESI) coupled to a multi-collector ICP-MS (Nu Instruments Plasma II). Ablation was made using He as carrier gas. The He carrier gas was mixed with the Ar carrier gas

flow prior to the ICP plasma torch. Depending on the CL zonation pattern of the zircons, either lines or spots were ablated. Line widths for rastering were 10 μm with a rastering speed of 5 μm/s. Energy densities were 5 J/cm^2 with a repetition rate of 10 Hz. Ablation duration was 30 to 70 s with a 30 s gas and Hg blank measurement preceding ablation. Ablation count rates were corrected accordingly offline. Remaining counts on mass 204 were interpreted as representing ^{204}Pb. Static mass spectrometer analysis was as follows: ^{238}U and ^{232}Th were measured on Faraday detectors, ^{208}Pb, ^{207}Pb, ^{206}Pb, ^{204}(Pb + Hg), and ^{202}Hg in ion counter detectors, respectively. An integration time of 1 s was used for all measurements. The ion counter – Faraday and inter-ion counter gain factors were determined before the analytical session using the reference zircon Plešovice (Sláma et al., 2008). The sensitivity for ^{206}Pb on reference zircon Plešovice was c. 30,000 cps/ppm Pb while for ^{238}U the corresponding value was c. 35,000 cps/ppm U.

U/Pb ratios were corrected for downhole-fractionation using the "intercept method" of Sylvester and Ghaderi (1997). The calculated ^{206}Pb/^{238}U and ^{207}Pb/^{206}Pb intercept values, respectively, were then corrected for mass discrimination from analyses of reference zircon Plešovice measured during the analytical session using a standard bracketing method (Klötzli et al., 2009). The correction utilizes regression of standard measurements by a quadratic function. A ^{204}Pb-based common Pb correction was applied to the data based on the amount of ^{204}Pb using the apparent ^{207}Pb/^{206}Pb age and the Stacey and Kramers Pb evolution model (Stacey and Kramers, 1975). Final age calculations were performed with Isoplot 3.0 (Ludwig, 2003). The zircon U-Pb data are reported in Table 3 and all uncertainties are at the 2-sigma level. Reference zircon Plešovice (Sláma et al., 2008) was also used as secondary reference material in order to test the overall reproducibility of the analytical method to constrain the external reproducibility (accuracy + precision + uncertainty). 15 measurements made during the analytical session resulted in a concordia age of 338.8 ± 2.6 Ma. This is within the assigned uncertainties of the accepted reference ^{206}Pb/^{238}U thermal ionization mass spectrometry (TIMS) date of 337.13 ± 0.37 Ma (Sláma et al., 2008).

3.6. Zircon rare earth element (REE) analyses

All zircon REE data were acquired using a Photon Machines Analyte Exite 193 nm ArF Excimer laser-ablation system with a Helex 2-volume ablation cell coupled to a Thermo Scientific iCAP Qc at Trinity College Dublin (TCD). 0.65 l/min He carrier gas was split evenly between the large outer sample chamber and the small inner volume (the "cup") where ablation occurs. A small volume of N_2 (ca. 6 ml/min) to enhance signal sensitivity and reduce oxide formation and 0.7 l/min Ar nebulizer gas were then introduced to the sample-gas mixture via an in-house smoothing device. The twenty-one isotopes (with the respective dwell times in milliseconds in parentheses) acquired were: ^{89}Y (5), ^{91}Zr (5), ^{139}La (50), ^{140}Ce (10), ^{141}Pr (30), ^{146}Nd (10), ^{147}Sm (6), ^{153}Eu (20), ^{157}Gd (5), ^{159}Tb (15), ^{163}Dy (5), ^{165}Ho (12.5), ^{166}Er (5), ^{169}Tm (10), ^{172}Yb (3.5), ^{175}Lu (7.5), ^{204}Pb (10), ^{206}Pb (40), ^{207}Pb (60), ^{232}Th (10), ^{238}U (30), with a total duty cycle of 378 ms. A 30 μm laser spot, a 5 Hz laser repetition rate and a fluence of 3.9 J/cm^2 were used, with a 45 s ablation period and a 25 s washout, the last 10 s of which were used for the baseline determination. The raw isotope data were reduced using the "Trace Elements" data reduction scheme of the freeware IOLITE package of Paton et al. (2011). NIST612 reference glass was used as the primary standard, with ^{91}Zr used as an internal standard. Sample-standard bracketing was then applied to account for long-term (session-wide) drift in isotopic or elemental ratios. 91,500 zircon (Wiedenbeck et al., 1995) and AusZ2 zircon (Kennedy et al., 2014) were used as secondary reference material controls for the zircon REE data. All zircon trace element data are listed in Supplementary Table 2.

3.7. LA-ICP-MS U-Pb dating and trace-element analyses of apatite and titanite

Apatite and titanite REE and U-Pb data were acquired using the Trinity College Dublin LA-ICP MS instrumentation described above. For apatite, twenty-eight isotopes (^{31}P, ^{35}Cl, ^{43}Ca, ^{55}Mn, ^{86}Sr, ^{89}Y, ^{139}La, ^{140}Ce, ^{141}Pr, ^{146}Nd, ^{147}Sm, ^{153}Eu, ^{157}Gd, ^{159}Tb, ^{163}Dy, ^{165}Ho, ^{166}Er, ^{169}Tm, ^{172}Yb, ^{175}Lu, ^{200}Hg, ^{204}Pb, ^{206}Pb, ^{207}Pb, ^{208}Pb, ^{232}Th, ^{238}U and mass 248(^{232}Th^{16}O) were acquired using a 50 μm laser spot, a 4 Hz laser repetition rate and a fluence of 3.31 J/cm^2. A c. 1 cm sized crystal of Madagascar apatite which has yielded a weighted average ID-TIMS concordia age of 473.5 ± 0.7 Ma (Cochrane et al., 2014) was used as the primary apatite reference material in this study. McClure Mountain syenite apatite (the rock from which the ^{40}Ar/^{39}Ar hornblende standard MMhb is derived) was used as a secondary standard. McClure Mountain syenite has moderate but reasonably consistent U and Th contents (~23 ppm and 71 ppm, Chew and Donelick, 2012) and its thermal history, crystallization age (weighted mean ^{207}Pb/^{235}U age of 523.51 ± 2.09 Ma) and initial Pb isotopic composition (^{206}Pb/^{204}Pb = 17.54 ± 0.24; ^{207}Pb/^{204}Pb = 15.47 ± 0.04) are known from high-precision TIMS analyses (Schoene and Bowring, 2006). NIST 612 standard glass was used as the apatite trace-element concentration reference material, and a crushed aliquot of Durango apatite that has been characterised by solution quadrupole-ICP-MS analyses (Chew et al., 2016) was used as the apatite trace-element secondary standard. For titanite, thirteen isotopes (^{43}Ca, ^{48}Ti, ^{89}Y, ^{90}Zr, ^{140}Ce, ^{172}Yb, ^{200}Hg, ^{204}Pb, ^{206}Pb, ^{207}Pb, ^{208}Pb, ^{232}Th, ^{238}U) were acquired using a 47 μm laser spot, a 5 Hz laser repetition rate and a fluence of 3.31 J/cm^2. The primary titanite standard used in this study is OLT1 titanite which has yielded a TIMS concordia age of 1014.8 ± 2.0 (Kennedy et al., 2010). BLR titanite Aleinikoff et al. (2002), which has yielded an ID-TIMS age of 1048.0 ± 0.7 Ma was used as the titanite secondary LA-ICP-MS age reference material.

The raw isotope data were reduced using a modified version of the "Vizual Age" data reduction scheme (Petrus and Kamber, 2012) of the freeware IOLITE package of Paton et al. (2011). This data reduction scheme ("VizualAge_UcomPbine") can account for variable common Pb in the apatite and titanite materials (Chew et al., 2014). User-defined time intervals are established for the baseline correction procedure to calculate session-wide baseline-corrected values for each isotope. The time-resolved fractionation response of individual standard analyses is then characterised using a user-specified down-hole correction model (such as an exponential curve, a linear fit or a smoothed cubic spline). The data reduction scheme then fits this appropriate session-wide "model" U-Th-Pb fractionation curve to the time-resolved standard data and the unknowns. Sample-standard bracketing is applied after the correction of down-hole fractionation to account for long-term drift in isotopic or elemental ratios by normalizing all ratios to those of the U-Pb reference standards. Common Pb in the apatite and titanite standards and unknowns was corrected using a ^{207}Pb-based correction in VizualAge_UcomPbine and includes the propagation of the uncertainties in the age of the standard materials. Over the course of two months of analyses, McClure Mountain apatite (^{207}Pb/^{235}U TIMS age of 523.51 ± 2.09 Ma; Schoene and Bowring, 2006) yielded a U-Pb Tera-Wasserburg concordia lower intercept age of 524.5 ± 3.7 Ma with an MSWD = 0.72. The lower intercept was anchored using a ^{207}Pb/^{206}Pb value of 0.88198 derived from an apatite ID-TIMS total U-Pb isochron (Schoene and Bowring, 2006). BLR titanite yielded a weighted average ^{207}Pb-corrected age of 1048 ± 11 (MSWD = 8.5). All apatite REE contents were normalized to C1 chondrite (Sun and McDonough, 1995). The apatite and titanite trace element data are listed in Supplementary Tables 3 and 4 respectively, while the apatite and titanite U-Pb data are provided in Tables 1 and 2.

Table 1
LA-ICP-MS U-Pb isotopic data of apatites from the Western Tatra Mountains.

Sample/spot	$^{207}Pb/^{235}Pb$	± 2σ	$^{206}Pb/^{235}U$	± 2σ	ρ	$^{238}U/^{206}Pb$	± 2σ	$^{207}Pb/^{206}Pb$	± 2σ	ρ	$^{206}Pb/^{238}U$ age	± 2σ Ma	$^{207}Pb/^{235}U$ age	± 2σ Ma	$^{207}Pb/^{206}Pb$ age	± 2σ Ma	^{207}Pb age	± 2σ Ma
Northern metamorphic cover																		
RW_1	8.46	0.39	0.12	0.0037	0.8944	8.0257	0.23	0.4820	0.011	−0.3974	757.0	21.0	2267	41	3050	310	360	11.00
RW_2	11.51	0.48	0.15	0.0044	0.9058	6.5531	0.19	0.5410	0.010	−0.4134	918.0	25.0	2553	39	3120	250	367	11.00
RW_3	32.10	1.00	0.33	0.0083	0.7390	3.0460	0.08	0.6820	0.012	0.0663	1829.0	40.0	3553	31	3460	400	431	30.00
RW_4	7.61	0.15	0.12	0.0023	0.4329	8.4388	0.16	0.4700	0.010	0.2947	722.0	13.0	2184	18	2930	320	353	14.00
RW_5	2.90	0.05	0.08	0.0008	0.3564	13.0141	0.14	0.2720	0.005	0.2860	477.2	4.9	1379	13	1980	300	348.9	5.40
RW_6	2.97	0.05	0.08	0.0008	0.4025	13.1579	0.13	0.2802	0.004	0.2444	472.2	4.6	1400	11	2240	310	340.5	5.10
RW_7	9.47	0.15	0.13	0.0016	0.3091	7.5358	0.09	0.5143	0.009	0.3755	804.3	8.9	2383	15	4100	470	352	12.00
RW_8	9.36	0.19	0.13	0.0015	0.2655	7.4738	0.09	0.5030	0.011	0.4246	809.6	8.7	2373	19	3540	210	366	14.00
RW_9	6.41	0.11	0.11	0.0011	0.4119	9.4251	0.10	0.4348	0.007	0.2220	650.2	6.5	2032	16	2970	370	343.2	8.30
RW_10	3.19	0.06	0.08	0.0009	0.3136	12.6231	0.14	0.2917	0.006	0.2394	491.4	5.3	1455	14	2220	260	348.7	5.80
RW_11	4.99	0.08	0.10	0.0012	0.3603	10.3734	0.13	0.3706	0.006	0.4247	593.2	7.0	1816	14	2280	390	362.8	7.70
RW_12	11.48	0.29	0.16	0.0025	0.7064	6.3211	0.10	0.5220	0.009	0.0235	946.0	14.0	2561	23	3180	280	409	13.00
RW_13	2.82	0.07	0.08	0.0013	0.6068	13.2979	0.24	0.2746	0.006	0.0869	467.4	8.0	1359	19	2160	320	337.1	7.10
RW_14	4.29	0.08	0.09	0.0008	0.3098	11.0939	0.09	0.3391	0.007	0.2257	556.4	4.7	1689	16	2470	300	361	6.30
RW_15	3.54	0.06	0.08	0.0011	0.2379	11.8483	0.15	0.3025	0.006	0.4503	522.3	6.6	1535	12	2700	250	362.4	7.00
RW_16	4.10	0.07	0.09	0.0011	0.4925	11.4679	0.15	0.3377	0.005	0.2820	538.8	6.7	1656	14	2820	220	350.9	6.00
RW_17	3.80	0.09	0.08	0.0012	0.6568	11.7786	0.16	0.3227	0.006	−0.0432	525.2	7.1	1589	18	2500	290	353.3	6.10
RW_18	3.50	0.06	0.08	0.0009	0.0983	12.0149	0.12	0.3013	0.005	0.5157	515.3	5.1	1526	13	2260	290	358.8	5.90
RW_19	3.68	0.10	0.08	0.0013	0.1042	11.7786	0.18	0.3130	0.009	0.4326	525.5	7.7	1568	21	2580	420	361	5.80
RW_20	3.85	0.15	0.08	0.0017	0.6547	11.8624	0.24	0.3290	0.011	0.0752	522.0	10.0	1599	30	2740	330	348	10.00
RW_21	4.38	0.07	0.09	0.0010	0.3906	11.0742	0.12	0.3496	0.005	0.2953	558.5	5.8	1706	14	2450	250	354.5	6.80
RW_22	3.67	0.06	0.08	0.0008	0.2764	11.9048	0.11	0.3146	0.005	0.2704	520.0	4.8	1564	12	2390	300	352.1	5.60
RW_23	3.31	0.07	0.08	0.0012	0.3131	12.3609	0.18	0.2933	0.006	0.3874	501.5	7.0	1481	17	2600	260	355.2	7.60
RW_24	4.26	0.09	0.09	0.0019	0.4040	10.9170	0.23	0.3331	0.009	0.4880	565.0	12.0	1684	18	2610	310	368	13.00
RW_25	4.37	0.09	0.09	0.0011	0.2258	11.1483	0.14	0.3518	0.007	0.3667	554.0	6.5	1710	17	2920	190	351.6	7.50
SM_1	11.77	0.34	0.15	0.0033	0.8564	6.5189	0.14	0.5570	0.009	−0.3383	920.0	18.0	2585	26	4120	600	345	11.00
SM_2	12.68	0.24	0.16	0.0027	0.5436	6.2893	0.11	0.5860	0.011	0.2877	953.0	15.0	2656	17	3260	450	323	16.00
SM_3	10.64	0.22	0.15	0.0024	0.3181	6.7568	0.11	0.5301	0.009	0.4550	889.0	14.0	2492	18	3140	310	371	14.00
SM_4	10.82	0.22	0.14	0.0024	0.4012	6.9061	0.11	0.5490	0.012	0.3179	871.0	13.0	2505	19	3460	270	337	16.00
SM_5	16.95	0.56	0.20	0.0041	0.7842	5.0505	0.10	0.6230	0.014	−0.1206	1164.0	22.0	2928	30	5130	360	350	22.00
SM_6	9.84	0.32	0.13	0.0029	0.5439	7.5472	0.16	0.5380	0.015	0.1255	802.0	16.0	2420	30	4870	580	321	18.00
SM_7	24.90	1.00	0.27	0.0077	0.9356	3.7693	0.12	0.6820	0.013	−0.1499	1516.0	39.0	3296	40	4330	640	360	26.00
SM_8	4.46	0.11	0.09	0.0013	0.3829	11.1359	0.16	0.3602	0.008	0.1811	554.2	7.6	1722	19	2820	270	345.5	8.30
SM_9	5.11	0.15	0.10	0.0015	0.4135	10.2459	0.17	0.3839	0.010	0.1435	600.3	8.8	1841	25	2850	290	360	10.00
SM_10	6.04	0.15	0.11	0.0013	0.3507	9.4967	0.12	0.4181	0.010	0.2573	645.3	7.6	1978	21	2930	390	358.7	9.60
SM_11	7.59	0.17	0.12	0.0016	0.4401	8.3195	0.10	0.4632	0.010	0.1859	731.4	9.0	2180	21	3510	440	367	11.00
SM_12	44.20	1.20	0.44	0.0097	0.8157	2.2805	0.05	0.7350	0.011	−0.1515	2342.0	44.0	3872	29	4890	430	380	38.00
SM_13	44.50	1.30	0.43	0.0110	0.8280	2.3148	0.06	0.7470	0.014	0.1469	2313.0	49.0	3869	30	4690	470	345	50.00
SM_14	60.00	2.10	0.55	0.0140	0.6283	1.8083	0.05	0.7830	0.021	0.1331	2835.0	58.0	4172	35	4760	330	293	91.00
SM_15	4.28	0.11	0.09	0.0016	0.6637	11.0375	0.20	0.3446	0.007	−0.0049	559.2	9.6	1689	22	2620	300	360.3	8.20
SM_16	4.38	0.09	0.09	0.0012	0.4076	11.1111	0.14	0.3550	0.007	0.2358	555.3	6.9	1711	17	2440	270	352.6	7.20
SM_17	4.26	0.08	0.09	0.0010	0.3634	11.2790	0.12	0.3499	0.006	0.2344	547.6	5.6	1683	15	2310	330	348.6	6.60
SM_18	8.50	0.18	0.13	0.0018	0.2423	7.9618	0.11	0.4935	0.009	0.2021	763.0	10.0	2290	18	3050	590	352	11.00
SM_19	5.77	0.12	0.10	0.0015	0.4687	9.8328	0.15	0.4129	0.008	0.2272	624.5	9.0	1942	19	2820	290	343.3	9.50
SM_20	5.86	0.10	0.10	0.0013	0.3746	9.8039	0.12	0.4197	0.007	0.3482	625.9	7.5	1954	14	2410	390	342.5	7.50
SM_21	30.54	0.92	0.32	0.0089	0.6729	3.1046	0.09	0.6870	0.016	0.3631	1798.0	43.0	3510	29	4890	380	410	46.00
SM_22	43.60	1.10	0.44	0.0092	0.4279	2.2957	0.05	0.7360	0.018	0.4039	2340.0	41.0	3852	24	5110	310	388	67.00
SM_23	29.39	0.81	0.32	0.0061	0.4546	3.1646	0.06	0.6870	0.017	0.2580	1769.0	30.0	3468	27	4600	420	394	42.00
SM_24	8.38	0.19	0.12	0.0021	0.5184	8.0580	0.14	0.4889	0.009	0.2909	754.0	12.0	2269	20	3040	340	352	13.00
SM_25	16.12	0.43	0.19	0.0036	0.5221	5.3135	0.11	0.6200	0.014	0.3215	1111.0	19.0	2882	26	4410	540	342	22.00
SM_26	9.78	0.20	0.13	0.0024	0.5690	7.5075	0.13	0.5287	0.010	0.3117	806.0	13.0	2414	18	3480	240	333	14.00
SM_27	7.19	0.17	0.12	0.0017	0.5772	8.6806	0.13	0.4548	0.009	0.1617	702.8	9.8	2132	21	3100	320	356	10.00
SM_28	10.68	0.32	0.15	0.0032	0.7122	6.7797	0.15	0.5280	0.011	0.0926	886.0	18.0	2501	27	3380	320	369	16.00

(*continued on next page*)

Table 1 (*continued*)

Sample/spot	$^{207}Pb/^{235}Pb$	± 2σ	$^{206}Pb/^{235}U$	± 2σ	ρ	$^{238}U/^{206}Pb$	± 2σ	$^{207}Pb/^{206}Pb$	± 2σ	ρ	$^{206}Pb/^{238}U$ age	± 2σ Ma	$^{207}Pb/^{235}U$ age	± 2σ Ma	$^{207}Pb/^{206}Pb$ age	± 2σ Ma	^{207}Pb age	± 2σ Ma
SM_29	19.54	0.60	0.22	0.0049	0.8287	4.6361	0.13	0.6480	0.015	0.0111	1259.0	26.0	3065	30	4150	490	343	25.00
SM_30	15.66	0.36	0.18	0.0028	0.6701	5.4735	0.09	0.6160	0.010	0.0596	1081.0	15.0	2855	22	3390	340	334	15.00
SM_31	7.85	0.20	0.12	0.0019	0.5015	8.2576	0.13	0.4698	0.010	0.1325	737.0	11.0	2216	22	2730	370	359	11.00
SM_32	6.37	0.15	0.11	0.0021	0.6840	9.3458	0.18	0.4309	0.009	0.0167	655.0	12.0	2024	21	2600	290	347	10.00
SM_33	4.21	0.10	0.09	0.0013	0.4274	11.2740	0.16	0.3447	0.007	0.1780	547.6	7.4	1675	19	2960	250	351.7	7.30
SM_34	10.99	0.22	0.15	0.0018	0.3239	6.7705	0.09	0.5410	0.011	0.3487	889.0	10.0	2519	18	3520	410	354	14.00
SM_35	16.44	0.34	0.19	0.0028	0.5551	5.1760	0.08	0.6220	0.010	0.2191	1139.0	15.0	2902	20	3530	240	346	18.00
SM_36	28.73	0.68	0.30	0.0049	0.5845	3.3322	0.05	0.6910	0.012	0.2513	1694.0	24.0	3443	23	4720	390	368	30.00
SM_37	16.14	0.26	0.19	0.0033	0.3829	5.1706	0.09	0.6050	0.011	0.5912	1142.0	17.0	2887	15	3710	370	370	21.00
SM_38	13.06	0.24	0.17	0.0020	0.1966	6.0459	0.08	0.5770	0.011	0.5169	987.0	11.0	2689	17	4280	460	354	17.00
SM_39	4.61	0.11	0.09	0.0014	0.3249	10.9649	0.16	0.3685	0.008	0.2525	562.4	8.0	1750	20	2520	230	344.2	9.20
SM_40	3.85	0.06	0.09	0.0008	0.2797	11.4969	0.11	0.3202	0.004	0.3431	537.6	4.9	1601	12	2380	240	361.5	4.80
SM_41	2.79	0.05	0.08	0.0007	0.4362	13.0157	0.12	0.2638	0.005	0.1048	477.2	4.3	1351	14	1940	270	353.8	4.20
SM_42	6.21	0.15	0.10	0.0016	−0.0961	9.5694	0.15	0.4320	0.011	0.7432	640.9	9.4	2006	22	2640	460	344	11.00
SM_43	4.41	0.09	0.09	0.0010	0.4994	11.1982	0.12	0.3594	0.006	0.1500	551.4	6.0	1712	17	2270	340	346.5	5.80
SM_44	7.29	0.17	0.11	0.0015	0.2606	8.7566	0.11	0.4610	0.011	0.2658	696.8	8.9	2143	21	2970	260	345	12.00
SM_45	6.51	0.11	0.11	0.0014	0.3243	9.3284	0.12	0.4362	0.007	0.3950	656.3	8.2	2045	15	2760	310	347.1	8.50
OR_1	5.63	0.18	0.10	0.0018	0.6834	9.8522	0.17	0.4030	0.011	−0.2001	623.2	11.1	1921	61	3920	107	360.2	10.60
OR_2	5.73	0.15	0.10	0.0018	0.2875	9.6525	0.16	0.3960	0.011	0.3736	635.5	11.0	1936	51	3894	108	373.1	10.79
OR_3	6.95	0.15	0.11	0.0016	0.4570	8.8028	0.12	0.4436	0.009	0.2481	693.6	9.8	2105	45	4064	79	367.1	9.03
OR_4	11.15	0.31	0.15	0.0032	0.3664	6.6357	0.15	0.5300	0.013	0.4069	904.9	19.2	2536	71	4327	106	385.3	16.98
OR_5	17.78	0.33	0.20	0.0030	0.5316	4.9603	0.075	0.6306	0.010	0.3322	1183.9	17.6	2978	55	4580	72	358.2	16.15
OR_6	25.24	0.49	0.27	0.0031	0.0345	3.7341	0.042	0.6770	0.014	0.4937	1529.6	17.7	3318	64	4683	97	378.7	28.96
OR_7	12.32	0.26	0.16	0.0025	0.4854	6.3735	0.098	0.5680	0.011	0.2654	939.5	15.0	2629	55	4428	86	355.3	14.34
OR_8	24.45	0.45	0.27	0.0037	0.3740	3.7693	0.053	0.6710	0.012	0.4029	1516.9	21.2	3287	60	4670	84	387.4	24.87
OR_9	23.74	0.44	0.26	0.0042	0.3880	3.8700	0.064	0.6620	0.012	0.4686	1481.7	24.1	3258	60	4650	84	395.2	24.48
OR_10	19.42	0.31	0.22	0.0027	0.1940	4.5579	0.058	0.6390	0.012	0.5625	1278.7	15.7	3063	49	4599	86	375.2	20.62
OR_11	4.67	0.11	0.09	0.0013	0.6495	11.0132	0.16	0.3710	0.006	−0.0984	560.3	8.0	1762	42	3796	65	345.1	6.59
OR_12	2.895	0.05	0.08	0.0008	0.5280	13.3103	0.13	0.2793	0.004	0.0472	467.0	4.7	1381	24	3359	42	339.3	3.89
OR_13	5.7	0.11	0.10	0.0015	0.4278	9.7466	0.15	0.3980	0.007	0.3622	629.6	9.2	1931	37	3902	69	368.0	7.62
OR_14	6.33	0.13	0.11	0.0014	0.4288	9.2593	0.12	0.4240	0.008	0.2366	661.1	8.6	2023	42	3996	74	365.5	8.02
OR_15	3.846	0.088	0.09	0.0013	0.3104	11.6279	0.18	0.3266	0.008	0.2904	531.8	8.0	1602	37	3601	86	356.4	7.38
OR_16	3.461	0.084	0.08	0.0013	0.0537	12.0192	0.19	0.2991	0.009	0.4945	515.2	8.0	1518	37	3466	102	362.5	7.90
OR_17	3.57	0.066	0.08	0.0015	0.2423	12.0773	0.2	0.3130	0.006	0.7149	512.8	9.3	1543	29	3536	70	352.0	7.40
OR_18	3.328	0.052	0.08	0.0010	0.5866	12.3457	0.16	0.2965	0.004	0.2221	502.1	6.2	1488	23	3452	47	354.7	4.97
OR_19	3.085	0.091	0.08	0.0017	0.6454	12.4378	0.27	0.2750	0.006	0.1010	498.5	10.5	1429	42	3335	75	365.4	8.49
OR_20	2.797	0.037	0.08	0.0007	0.5100	13.1822	0.12	0.2683	0.004	0.2149	471.4	4.2	1355	18	3296	44	349.0	3.72
OR_21	5.94	0.17	0.11	0.0016	0.4213	9.4697	0.14	0.4002	0.010	0.0405	647.1	9.8	1967	56	3910	93	376.7	9.50
OR_22	4.491	0.095	0.09	0.0013	0.3914	10.9769	0.15	0.3604	0.007	0.3021	562.0	8.0	1729	37	3752	74	353.6	7.01
OR_23	7.54	0.34	0.12	0.0034	0.8775	8.6207	0.26	0.4730	0.012	−0.4488	707.5	20.7	2178	98	4159	106	348.6	14.65
OR_24	2.098	0.048	0.07	0.0008	0.4185	14.2694	0.17	0.2166	0.004	0.0836	436.6	5.0	1148	26	2956	60	350.6	4.63
OR_25	2.61	0.062	0.07	0.0008	0.4678	13.3690	0.15	0.2513	0.005	0.0336	465.0	5.2	1303	31	3193	69	353.9	4.95
AMB1_1	2.68	0.08	0.06	0.0013	0.5780	15.7729	0.32	0.3110	0.011	0.1761	396.2	8.1	1321	22	3790	470	272.8	9.10
AMB1_2	32.41	0.92	0.32	0.0085	0.5519	3.1085	0.08	0.7360	0.020	0.3580	1801.0	41.0	3564	26	5120	160	280	56.00
AMB1_3	13.03	0.33	0.14	0.0030	0.6677	7.1174	0.16	0.6670	0.012	0.2618	849.0	17.0	2681	23	5090	360	200	14.00
AMB1_4	63.10	3.50	0.57	0.0300	0.9256	1.7483	0.09	0.7900	0.012	0.1841	2900.0	130.0	4208	58	4000	470	251	53.00
AMB1_5	2.33	0.10	0.06	0.0015	0.8993	15.6740	0.37	0.2649	0.008	−0.5893	398.7	9.2	1215	28	2830	300	292	7.60
AMB1_6	35.50	2.30	0.34	0.0220	0.9590	2.9155	0.19	0.7630	0.013	−0.0081	1890.0	100.0	3624	65	4780	370	222	39.00
AMB1_7	2.92	0.11	0.07	0.0015	0.7315	14.8148	0.33	0.3141	0.009	−0.1867	421.2	8.9	1387	30	3080	250	283.3	6.90
AMB1_8	4.56	0.16	0.07	0.0017	0.5641	14.9254	0.38	0.4910	0.015	−0.1665	418.0	10.0	1734	29	4530	340	193	11.00
AMB1_9	4.83	0.14	0.06	0.0014	0.4993	16.2075	0.37	0.5720	0.015	0.3329	386.1	8.5	1785	24	4710	270	131.2	8.80
AMB2_1	13.61	0.46	0.16	0.004	0.4657	6.3980	0.18	0.618	0.022	0.32931	936.2	26.4	2723	92	4551	162	290.7	28.74
AMB2_5	5.88	0.25	0.09	0.002	0.6582	10.8932	0.27	0.472	0.017	0.2072	566.2	14.8	1958	83	4156	150	275.8	14.40
AMB2_18	10.16	0.32	0.13	0.003	0.6408	7.7760	0.17	0.584	0.013	0.052733	779.9	17.0	2449	77	4469	99	272.9	15.32
AMB2_19	9.90	1.20	0.12	0.009	0.9656	8.0128	0.57	0.561	0.032	−0.54002	758.1	55.3	2426	294	4410	252	287.9	37.57

(*continued on next page*)

Table 1 (*continued*)

Sample/spot	$^{207}Pb/^{235}Pb$	± 2σ	$^{206}Pb/^{235}U$	± 2σ	ρ	$^{238}U/^{206}Pb$	± 2σ	$^{207}Pb/^{206}Pb$	± 2σ	ρ	$^{206}Pb/^{238}U$ age	± 2σ Ma	$^{207}Pb/^{235}U$ age	± 2σ Ma	$^{207}Pb/^{206}Pb$ age	± 2σ Ma	^{207}Pb age	± 2σ Ma
AMB2_33	3.41	0.16	0.07	0.002	0.8244	14.5560	0.40	0.373	0.013	−0.29182	428.3	12.5	1507	71	3804	133	259.8	10.36
AMB2_34	21.27	0.53	0.23	0.005	0.3055	4.3328	0.10	0.682	0.021	0.44459	1338.7	31.3	3151	79	4693	145	315.3	39.87
AMB2_26	3.08	0.08	0.08	0.0012	0.0021	13.2275132	0.21	0.3055	0.009	0.5473	469.8	7.5	1427	38	3498	103	326.0	7.47
AMB2_27	4.63	0.17	0.09	0.002	0.6512	10.9890	0.24	0.382	0.012	0.15167	561.4	12.3	1755	64	3840	121	338.0	11.38
AMB2_28	10.50	1.20	0.14	0.010	0.9650	6.9930	0.50	0.518	0.021	−0.78621	861.6	60.3	2480	283	4293	174	380.6	35.14
AMB2_29	5.17	0.17	0.10	0.002	0.3213	10.0908	0.17	0.392	0.011	0.24856	609.1	9.8	1848	61	3879	109	360.5	10.47
AMB2_36	9.63	0.56	0.13	0.005	0.8627	7.5472	0.26	0.532	0.015	−0.31712	802.1	27.8	2400	140	4332	122	337.1	19.80
AMB2_37	6.22	0.18	0.10	0.002	−0.0222	9.5694	0.18	0.44	0.014	0.55516	640.7	12.3	2007	58	4052	129	340.9	13.34
AMB2_6	10.46	0.33	0.14	0.0034	0.3367	7.27802038	0.17	0.546	0.017	0.39057	829.9	20.5	2476	78	4370	136	334.5	20.46
AMB2_7	14.83	0.41	0.18	0.004	0.3583	5.5960	0.12	0.612	0.016	0.33796	1059.9	23.7	2804	78	4537	119	343.4	24.58
AMB2_15	16.84	0.53	0.19	0.005	0.7549	5.2466	0.14	0.644	0.014	0.18011	1124.6	31.3	2926	92	4611	100	317.2	24.15
AMB2_21	17.50	1.50	0.20	0.008	−0.0861	5.0403	0.19	0.651	0.053	0.16671	1166.7	48.8	2963	254	4626	377	319.4	82.59
AMB2_22	3.08	0.08	0.08	0.001	0.0021	13.2275	0.21	0.3055	0.009	0.5473	469.8	7.5	1427	38	3498	103	326.0	7.47
AMB2_23	4.63	0.17	0.09	0.002	0.6512	10.989011	0.24	0.382	0.012	0.15167	561.4	12.3	1755	64	3840	121	338.0	11.38
AMB2_30	10.50	1.20	0.14	0.01	0.9650	6.99300699	0.5	0.518	0.021	−0.78621	861.6	60.3	2480	283	4293	174	380.6	35.14
AMB2_31	5.17	0.17	0.10	0.0016	0.3213	10.0908174	0.17	0.392	0.011	0.24856	609.1	9.8	1848	61	3879	109	360.5	10.47
AMB2_34	21.27	0.53	0.23	0.005	0.3055	4.3328	0.10	0.682	0.021	0.44459	1338.7	31.3	3151	79	4693	145	315.3	39.87

4. Results

Fig. 2

4.1. Petrography and geochemistry

All four amphibolite samples exhibit a strong tectonic foliation and lineation, as peak metamorphism was contemporaneous with shearing and *syn*-tectonic granitoid emplacement.

Migmatized amphibolite from Smreczyński Wierch (SM). Sample SM is characterised by intercalations of dark, amphibole-rich layers and leucocratic plagioclase-quartz leucosomes which together define the main foliation. The main rock-forming minerals are ferro-hornblende to ferroan tchermakitic hornblende (Supplementary Table 5, weakly zoned oligoclase-andesine plagioclase ($An_{38–35}$ in the cores to $An_{26–13}$ at rims), quartz, ilmenite ($(Ti_{0.99}V_{0.01}Fe_{0.96–0.95}Mn_{0.04–0.05}O_3$; Supplementary Table 6) and fluorapatite (Supplementary Table 7). Zircon was present as an accessory phase.

The chemical composition of this amphibolite corresponds to the suite 1 amphibolites defined by Gawęda et al. (2000), with Zr/Y ~ 4, ΣREE = 102.87, flat chondrite (C1)-normalized REE patterns with Ce_N/Yb_N = 2.17 and Eu/Eu* = 0.8 (Supplementary Table 1). The protolith of these amphibolites are interpreted as mantle plume-related tholeiites.

Massive amphibolite from the Ornak Zone (OR). Sample OR is characterised by a pronounced metamorphic lineation and foliation. The main rock-forming minerals are Mg-hornblende (Supplementary Table 5), zoned andesine plagioclase ($An_{49–39}$), quartz, ilmenite ($(Ti_{0.99}V_{0.01}Fe_{0.98}Mn_{0.02}O_3$; Supplementary Table 6) and fluorapatite (Supplementary Table 7). Rare zircon crystals yield U-Pb core ages of 564 ± 8 Ma, while two generations of zircon growth on the rims have been dated at 387 ± 8 Ma (inner rim) and 342 ± 9 Ma (outer rim) (Gawęda et al., 2016b; Gawęda et al., 2017). Whole rock geochemistry data suggest the magmatic precursors are MORB-like basalts (Gawęda et al., 2017), with low Zr contents, low ΣREE (~80 ppm), flat chondrite (C1)-normalized REE patterns with Ce_N/Yb_N = 2.14 and Eu/Eu* = 0.91 (Supplementary Table 1).

The biotite paragneiss sample (sample RW) is composed of oligoclase plagioclase, biotite (*#mg* = 0.40–0.38; Ti = 0.30–0.31 a.p.f.u.; Supplementary Table 8), quartz and K-feldspar. Muscovite associated with late shearing has been dated by the K-Ar method at 317–298 Ma (Deditius, 2004). Secondary chlorite replacing biotite is abundant. Apatite and zircon are present as accessory phases. Zircon crystals were either metamict or too small for analysis (many zircon grains are at the micron-scale), and hence apatite was the only accessory phase on which U-Pb dating was undertaken. The whole rock geochemistry of this paragneiss resembles that of pelites from the Upper Structural Unit (Gawęda and Burda, 2004). The chondrite-normalized REE pattern of the paragneiss is characterised by weak LREE enrichment (Ce/Yb = 5.65), and a slightly positive Eu anomaly (Eu/Eu* = 1.88; Supplementary Table 1).

Striped and massive coarse grained amphibolites from the southern metamorphic envelope (samples AMB-1 and AMB-2) are composed mainly of Mg-hornblende, overgrown by actinolite, unzoned plagioclase ($An_{34–25}$) rimmed by albite, quartz and apatite. Sample AMB-1 also contains ilmenite and significant secondary epidote (Supplementary Table 9), while sample AMB-2 contains titanite underlining the metamorphic foliation (Figs. 2a,c,d), zoizite and secondary REE-bearing epidote (Supplementary Table 9; Fig. 2b). The rutile inclusions present in some of the titanite crystals show chemical heterogeneity (Fig. 2d) as shown by the heterogeneous Nb, Cr and V concentrations (Supplementary Table 6). The titanite exhibits minor chemical zonation in terms of V and Fe (Fig. 2d; Supplementary Table 10), which may also have been inherited from the rutile precursor. These amphibolites show low ΣREE contents, low to medium Zr contents, slight LREE enrichment (Ce_N/Yb_N = 2.73 and 4.26) and

Table 2
. LA-ICP-MS U-Pb isotopic data of titanits from the Western Tatra Mountains.

Sample/spot	$^{207}Pb/^{235}U$	± 2σ	$^{206}Pb/^{238}U$	± 2σ	ρ	$^{238}U/^{206}Pb$	± 2σ	$^{207}Pb/^{206}Pb$	± 2σ	ρ	$^{206}Pb/^{238}U$ age
Tnt_1	5.14	0.32	0.0903	0.0037	0.36	11.07	0.47	0.407	0.025	0.36	557
Tnt_2	2.33	0.15	0.0695	0.0017	0.08	14.39	0.37	0.241	0.012	0.42	433
Tnt_3	5.71	0.37	0.0955	0.0035	0.48	10.47	0.39	0.420	0.022	0.038	588
Tnt_4	5.76	0.39	0.0989	0.0037	0.40	10.11	0.39	0.407	0.027	0.24	608
Tnt_5	4.30	0.22	0.0900	0.0029	0.21	11.11	0.35	0.351	0.019	0.39	556
Tnt_6	5.99	0.77	0.1003	0.0068	0.71	9.97	0.67	0.369	0.031	−0.298	616
Tnt_7	34.6	1.7	0.326	0.014	0.49	3.07	0.13	0.763	0.036	0.51	1819
Tnt_8	2.85	0.17	0.0757	0.0023	0.045	13.21	0.42	0.277	0.018	0.45	470
Tnt_9	24.2	1.6	0.263	0.014	0.85	3.80	0.22	0.662	0.036	0.41	1505
Tnt_10	12.37	0.84	0.1578	0.0075	0.86	6.34	0.34	0.567	0.031	0.21	945
Tnt_11	16.1	1.2	0.195	0.011	0.44	5.13	0.31	0.610	0.043	0.40	1148
Tnt_12	4.60	0.24	0.0887	0.0027	0.28	11.27	0.34	0.363	0.018	0.36	548
Tnt_13	9.67	0.50	0.1331	0.0046	0.13	7.51	0.27	0.520	0.031	0.54	806
Tnt_14	1.82	0.10	0.0664	0.0014	0.46	15.06	0.32	0.200	0.01	−0.035	414
Tnt_15	3.43	0.16	0.0814	0.0021	0.29	12.29	0.31	0.307	0.014	0.35	504
Tnt_16	4.26	0.60	0.089	0.005	0.97	11.19	0.39	0.316	0.021	−0.49	552
Tnt_17	6.39	0.31	0.1068	0.0036	0.33	9.36	0.33	0.433	0.022	0.33	654
Tnt_18	4.07	0.20	0.0833	0.0025	0.10	12.00	0.36	0.353	0.020	0.47	516
Tnt_19	24.9	1.7	0.268	0.014	0.50	3.73	0.21	0.684	0.040	0.31	1531
Tnt_20	21.8	1.2	0.23	0.01	0.39	4.3	0.2	0.680	0.040	0.53	1340
Tnt_21	2.25	0.13	0.0700	0.0018	0.21	14.29	0.38	0.232	0.013	0.21	436
Tnt_22	16.0	1.0	0.206	0.011	0.20	4.9	0.3	0.615	0.048	0.65	1207
Tnt_23	3.27	0.19	0.0819	0.0024	0.059	12.21	0.36	0.299	0.018	0.45	507
Tnt_24	7.04	0.37	0.1145	0.0042	0.13	8.73	0.34	0.450	0.026	0.49	699
Tnt_25	7.08	0.47	0.1114	0.0052	0.36	8.98	0.43	0.470	0.032	0.43	681
Tnt_26	5.68	0.29	0.0959	0.0032	0.13	10.43	0.35	0.445	0.028	0.54	590
Tnt_27	3.58	0.29	0.0833	0.0034	0.44	12.00	0.48	0.323	0.026	0.28	516
Tnt_28	2.14	0.10	0.0699	0.0017	0.23	14.31	0.36	0.216	0.010	0.31	436
Tnt_29	20.5	2.3	0.227	0.020	0.97	4.41	0.33	0.634	0.025	−0.10	1319
Tnt_30	8.43	0.47	0.1252	0.0047	0.22	7.99	0.30	0.504	0.030	0.35	760
Tnt_31	17.4	1.2	0.198	0.011	0.87	5.05	0.25	0.661	0.034	0.13	1165
Tnt_32	42.0	2.6	0.419	0.022	0.37	2.39	0.13	0.748	0.048	0.50	2256
Tnt_33	2.68	0.12	0.072	0.002	0.18	13.81	0.38	0.269	0.013	0.34	451
Tnt_34	122.9	6.6	1.087	0.053	0.70	0.920	0.048	0.817	0.034	0.35	4743
Tnt_35	14.43	0.76	0.176	0.007	0.27	5.69	0.25	0.608	0.035	0.62	1043
Tnt_36	14.7	1.1	0.1769	0.0099	0.89	5.65	0.30	0.608	0.024	−0.024	1050
Tnt_37	251	27	2.19	0.26	0.94	0.46	0.06	0.919	0.072	0.47	7478
Tnt_38	226	25	2.08	0.27	0.81	0.48	0.06	0.935	0.088	0.069	7252
Tnt_39	8.94	0.44	0.1302	0.0047	0.27	7.68	0.28	0.500	0.028	0.57	789
Tnt_40	4.39	0.22	0.0871	0.0028	0.016	11.48	0.38	0.374	0.023	0.59	538
Tnt_41	94.6	4.9	0.845	0.037	0.80	1.183	0.051	0.807	0.026	0.12	3948
Tnt_42	81.4	6.2	0.745	0.052	0.52	1.34	0.11	0.804	0.058	0.54	3589
Tnt_43	8.41	0.45	0.1302	0.0045	0.070	7.68	0.28	0.472	0.030	0.497	789
Tnt_44	78.3	4.0	0.711	0.036	0.38	1.406	0.073	0.837	0.049	0.56	3462
Tnt_45	48.4	2.7	0.440	0.021	0.55	2.27	0.11	0.798	0.041	0.51	2351
Tnt_46	89.9	6.7	0.800	0.053	0.78	1.250	0.094	0.821	0.054	0.597	3789
Tnt_47	17.8	1.7	0.194	0.013	0.91	5.15	0.36	0.629	0.033	−0.0046	1143
Tnt_48	3.11	0.16	0.0754	0.0021	0.37	13.26	0.38	0.292	0.014	0.26	469
Tnt_49	10.52	0.63	0.1398	0.0061	0.24	7.15	0.36	0.560	0.037	0.48	844
Tnt_50	13.59	0.66	0.1630	0.0070	0.20	6.13	0.28	0.622	0.038	0.68	973
Tnt_51	252	32	2.01	0.28	0.88	0.498	0.096	0.950	0.086	0.46	7104
Tnt_52	39.2	4.4	0.391	0.035	0.94	2.56	0.24	0.725	0.042	0.39	2127
Tnt_53	12.38	0.68	0.1536	0.0068	0.59	6.51	0.29	0.594	0.029	0.38	921
Tnt_54	33.9	2.0	0.328	0.016	0.39	3.05	0.16	0.762	0.049	0.48	1829

(*continued on next page*)

Table 2 (*continued*)

Sample/spot	$^{207}Pb/^{235}U$	± 2σ	$^{206}Pb/^{238}U$	± 2σ	ρ	$^{238}U/^{206}Pb$	± 2σ	$^{207}Pb/^{206}Pb$	± 2σ	ρ	$^{206}Pb/^{238}U$ age
Tnt_55	52.9	4.4	0.47	0.03	0.7	2.12	0.13	0.786	0.050	0.27	2488
Tnt_56	1.735	0.077	0.067	0.0014	0.12	14.84	0.32	0.1878	0.0091	0.37	420
Tnt_57	6.34	0.29	0.11	0.0035	0.28	9.47	0.32	0.429	0.021	0.44	647
Tnt_58	18.2	3.9	0.21	0.034	0.98	4.83	0.71	0.493	0.032	−0.50	1213
Tnt_59	3.42	0.17	0.079	0.0023	−0.054	12.59	0.37	0.316	0.019	0.52	493

Sample/spot	± 2σ Ma	$^{207}Pb/^{235}U$ age	± 2σ Ma	$^{207}Pb/^{206}Pb$ age	± 2σ Ma	^{207}Pb age	± 2σ Ma	Pb_{tot} (ppm)	Th_{tot} (ppm)	U_{tot} (ppm)
Tnt_1	23	1843	115	3935	242	318	22	78	1.8	5.4
Tnt_2	11	1221	52	3127	156	335	10	134.1	16.8	15.6
Tnt_3	22	1933	125	3982	209	327	20	108	2.1	8.1
Tnt_4	23	1940	131	3935	261	348	24	76.1	1.5	5.4
Tnt_5	18	1693	87	3711	201	356	17	100.5	4.4	6.9
Tnt_6	42	1974	254	3787	318	382	35	77.1	0.7	8.5
Tnt_7	78	3627	178	4854	229	245	91	152.3	0.19	1.8
Tnt_8	14	1369	82	3346	217	343	15	83.9	2.8	10.7
Tnt_9	80	3276	217	4650	253	402	75	117.2	0.63	1.7
Tnt_10	45	2633	179	4426	242	359	41	98.2	0.7	3.1
Tnt_11	65	2883	215	4532	319	377	67	76.4	0.39	1.9
Tnt_12	17	1749	91	3762	187	343	16	138.3	11.2	8.2
Tnt_13	28	2404	124	4299	256	351	34	90.7	0.76	3.8
Tnt_14	9	1053	58	2826	141	341	9	142.8	8.7	26.5
Tnt_15	13	1511	70	3506	160	350	12	135.6	4.2	14.7
Tnt_16	31	1686	237	3550	236	377	25	166	2.7	14.8
Tnt_17	22	2031	99	4028	205	354	21	88.4	0.89	5.1
Tnt_18	15	1648	81	3720	211	329	16	101.2	2.2	9.5
Tnt_19	80	3304	226	4697	275	365	84	104	0.23	1.5
Tnt_20	58	3175	175	4689	276	322	72	89.3	0.36	1.7
Tnt_21	11	1197	69	3066	172	342	11	82.6	4.7	14.6
Tnt_22	64	2877	180	4544	355	390	78	75.6	0.38	1.7
Tnt_23	15	1474	86	3465	209	357	15	115.1	7.2	10.2
Tnt_24	26	2116	111	4085	236	364	26	82.8	1.8	4.1
Tnt_25	32	2122	141	4150	283	338	31	70.3	2.7	3.76
Tnt_26	20	1928	98	4069	256	310	23	101.8	5.1	5.6
Tnt_27	21	1545	125	3584	289	348	22	73.2	1	9.45
Tnt_28	11	1162	54	2951	137	350	10	125.1	11.5	17.4
Tnt_29	116	3115	350	4588	181	397	55	346.0	0.80	6.4
Tnt_30	29	2278	127	4253	253	346	31	87.4	0.99	4
Tnt_31	65	2957	204	4648	239	306	54	186	0.84	4.1
Tnt_32	118	3819	236	4826	310	361	155	82.1	0.58	0.73
Tnt_33	12	1323	59	3300	159	333	12	147.3	12.5	14.5
Tnt_34	231	4894	263	4952	206	354	283	226.0	0.05	0.71
Tnt_35	42	2778	146	4527	261	343	49	87.3	0.304	2.4
Tnt_36	59	2796	209	4527	179	346	38	292.0	1.3	7.3
Tnt_37	888	5614	604	5118	401	−1117	1445	80.3	0	0.14
Tnt_38	941	5508	609	5143	484	−1365	1739	72.3	0.014	0.14
Tnt_39	28	2332	115	4241	238	364	31	92.4	0.54	3.7
Tnt_40	17	1710	86	3808	234	329	19	93	2.3	8.1
Tnt_41	173	4630	240	4934	159	341	169	418	0.93	1.7
Tnt_42	251	4479	341	4929	356	319	333	73.8	0.13	0.35
Tnt_43	27	2276	122	4156	264	392	33	80.6	0.39	4
Tnt_44	175	4441	227	4986	292	122	273	96.8	0.07	0.47
Tnt_45	112	3960	221	4918	253	210	140	140.8	0.11	1.2
Tnt_46	251	4579	341	4959	326	237	335	87.3	0.21	0.39
Tnt_47	77	2979	285	4576	240	347	54	149	0.59	3.5

(*continued on next page*)

Table 2 (*continued*)

Sample/spot	± 2σ Ma	$^{207}Pb/^{235}U$ age	± 2σ Ma	$^{207}Pb/^{206}Pb$ age	± 2σ Ma	^{207}Pb age	± 2σ Ma	Pb_{tot} (ppm)	Th_{tot} (ppm)	U_{tot} (ppm)
Tnt_48	13	1435	74	3428	164	333	12	121.6	7.9	13.1
Tnt_49	37	2482	149	4407	291	326	42	87.1	1.6	2.8
Tnt_50	42	2722	132	4560	279	301	49	81.6	0.41	2.2
Tnt_51	990	5619	713	5165	468	−1603	1706	55.9	0.07	0.12
Tnt_52	190	3751	421	4781	277	406	130	110	0.34	1
Tnt_53	41	2634	145	4493	219	317	37	133.4	0.66	3.9
Tnt_54	89	3607	213	4852	312	249	125	90.9	0.12	1
Tnt_55	158	4048	337	4897	311	268	183	88.3	0.14	0.71
Tnt_56	9	1022	45	2723	132	352	9	267.8	49.6	26.9
Tnt_57	21	2024	93	4014	196	353	21	105.2	2.5	6.3
Tnt_58	199	3000	643	4220	274	583	106	334	2.8	7.8
Tnt_59	14	1509	75	3550	213	336	15	103.4	4.8	10.2

negligible Eu anomalies (Eu/Eu* = 0.89 and 0.98; Supplementary Table 1).

4.2. *P-T conditions of metamorphism*

The migmatitic amphibolites (SM sample) underwent anatexis with associated leucosome development. The cores of amphiboles in the trondhjemitic leucosomes yield pressures of 440–520 MPa based on estimates using the Schmidt (1992) barometer while a temperature of 715–768 °C was calculated using the Blundy and Holland (1990) amphibole-plagioclase geothermometer. Using these same geothermometer and geobarometers, the OR massive amphibolite, which exhibits evidence of marked partial melting, yields a higher peak pressure of 740 MPa, yet similar temperatures of 740–750 °C. The Ti-in-biotite geothermometer (after Henry et al., 2005) applied to the RW biotite paragneiss sample yielded temperatures of 645–650 °C (Supplementary Table 8), interpreted as a temperature estimate on the retrograde cooling path. These data are in agreement with earlier temperature estimates of 650–780 °C and pressure estimates of 750–900 MPa (Gawęda and Burda, 2004) for the metapelitic country rock hosting the amphibolite horizons, and with clockwise *P-T* paths for the southern part of the Western Tatra metamorphic complex (Moussallam et al., 2012 and references therein). The thermal metamorphic peak is likely associated with the prolonged emplacement of the polygenetic Tatra granitoid intrusion, which kept peak temperatures in the 750–800 °C range (Gawęda et al., 2016a). Subsequent cooling following granitoid magma emplacement is likely linked to heterogeneous extrusion of the metamorphic crystalline basement (Fig. 3; Janák et al., 1996). A significant pressure drop has been documented in post-magmatic/subsolidus mineral assemblages in the Western Tatra Mountains granite (pressure of c. 350–300 MPa at 660–470 °C; Gawęda and Włodyka, 2013; Fig. 3).

4.3. *Apatite trace element systematics and U-Pb chronology*

Apatite crystals from the amphibolites and the one paragneiss sample are classified as fluorapatite, with 2.72–3.63 wt% F (0.72–0.97 F atoms in the monovalent anion *Z*-site, which is occupied by OH^- or the halogens F^-, Cl^-; Supplementary Table 7).

Fluorapatites from the northern portion of the metamorphic envelope (samples SM, OR and RW) yield Sr contents from 117 to 398 ppm (mean: 224 ppm), Y contents from 80 to 423 ppm (mean: 186 ppm) and Mn contents from 297 to 1521 ppm. U/Th ratios show a very large range from 1.19 to 152 (Supplementary Table 3).

Fluorapatite crystals from the southern part of the metamorphic envelope (AMB-1 and AMB-2) yield Sr contents from 134 to 311 ppm (mean: 218 ppm) and Mn contents from 267 to 665 ppm (mean: 387 ppm; Supplementary Table 3) that are indicative of a metamorphic origin (cf. EL Korh et al., 2009). U/Th ratios range from 2.58 to 32.13 (Supplementary Table 3). However, in sample AMB-1, the Y contents range from 1198 to 6443 ppm (mean: 4027 ppm) while in sample AMB-2 much lower Y concentrations are observed (40 to 303 ppm; mean: 140 ppm). No optical and trace-element zonation was noted in any of the analysed apatites.

Apatite chondrite (C1)-normalized REE patterns differ between the northern and southern portions of the metamorphic cover. The three samples from the northern part of the metamorphic complex (samples SM, Or and RW) are dominated by weak REE fractionation (Ce_N/Yb_N = 0.8–10.9), negative Eu anomalies (Eu/Eu* = 0.43–0.82) and positive Ce anomalies (Ce/Ce* = 3.2–10.9; Supplementary Table 3, Fig. 4a, b, c). Apatite from sample AMB-1 from the southern portion of the metamorphic envelope exhibits enrichment in HREE (Ce_N/Yb_N = 0.06–0.17), with pronounced negative Eu anomalies (Eu/Eu* = 0.29–0.37) and no Ce anomaly (Supplementary Table 3; Fig. 5a). Apatite crystals from sample AMB-2 are split into 3 sub-populations based on their trace-element compositions (Supplementary Table 3): a

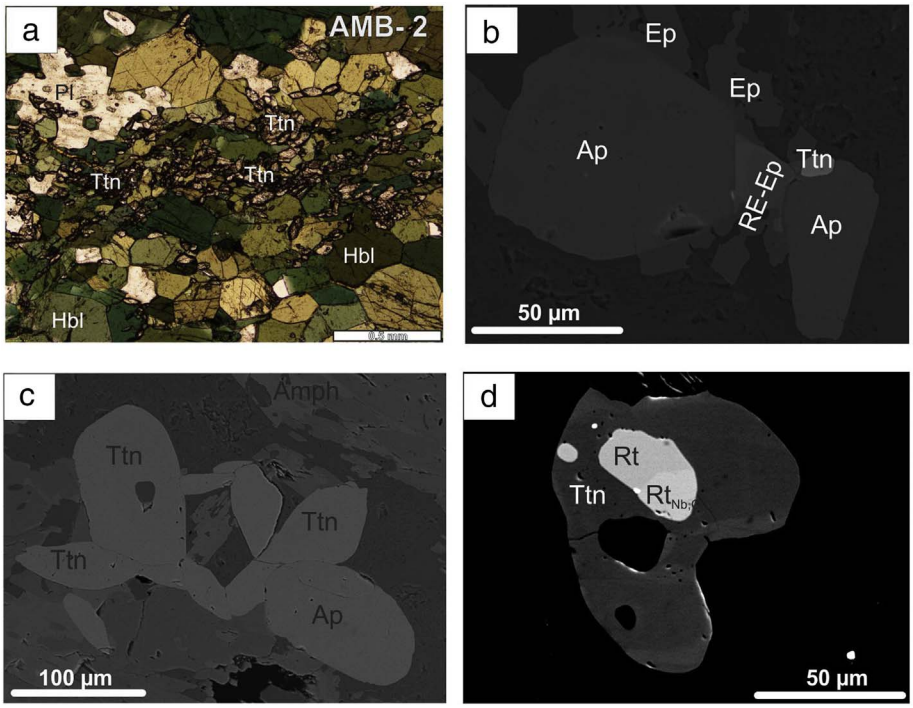

Fig. 2. A. Photomicrograph showing titanite crystals aligned along the foliation in AMB-2. B. BSE image of an apatite (Ap) coexisting with RE-bearing epidote (RE-ep) overgrown by late epidote (Ep) from sample AMB-1; C. BSE image of titanite (Ttn) and apatite (Ap1) from the AMB-2 amphibolite; D. BSE image of a zoned titanite (Ttn) crystal with a heterogeneous rutile (Rt) inclusion (zoned in Nb, Cr and V).

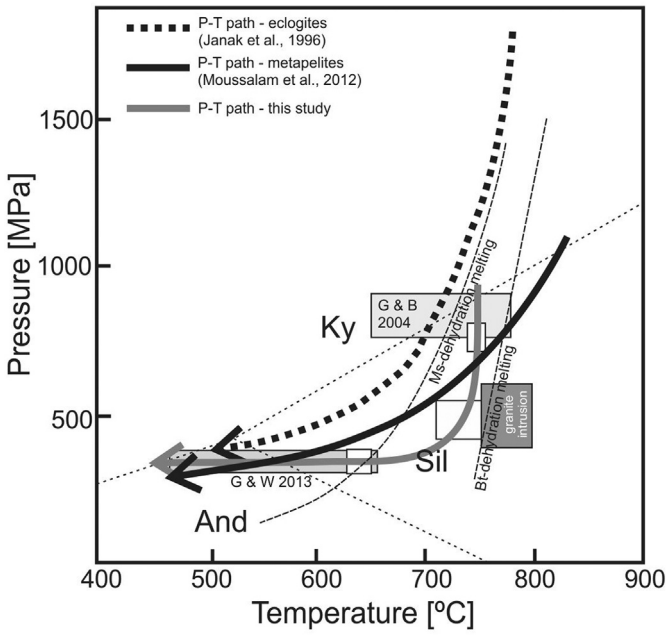

Fig. 3. *P-T* path illustrating the metamorphic evolution of the Western Tatra metamorphic complex. For comparison the P-T paths of Janák et al., 1996 and Moussallam et al., 2012 are also presented. Dashed lines represent the stability fields of kyanite (Ky), sillimanite (Sil) and andalusite (And) along with the common muscovite and biotite dehydration melting reactions. A white rectangle marks the *P-T* data from this study, a grey rectangle marks the Tatra Granite emplacement P-T conditions from Gawęda et al., 2016a; G & B 2004 – P-T data from Gawęda and Burda, 2004, G & W 2013 – PT data from Gawęda and Włodyka, 2013.

subpopulation (Ap1) with very low Y contents, weak LREE enrichment and flat chondrite-normalized REE profiles (Ce_N/Yb_N = 5.09–7.21; Eu/Eu* = 0.83–1.21), a second subpopulation (Ap2) with total REE contents in the range of 701–883 ppm, very flat chondrite-normalized REE profiles (Ce_N/Yb_N = 2.91–3.77) and negative Eu anomalies (Eu/Eu* = 0.66–0.78), and a third subpopulation (Ap3), which has very similar trace element characteristics to Ap2 with much lower LREE, Th and Mn contents and higher Sr-contents (Sm/La = 1.54–7.08; Eu/Eu* = 0.60–0. 77; Ce/Ce* = 1.16–1.35; Supplementary Table 3; Fig. 5b). The petrogenesis of these different apatite sub-populations in sample AMB-2 is discussed is Section 5.2.

LA-ICP-MS U-Pb apatite ages, calculated from unanchored Tera-Wasserburg lower intercepts, were determined for all three samples from the northern metamorphic cover. Each concordia clearly yields just one age population based on the well-constrained discordia intercepts (Fig. 6a–c), but the slightly elevated MSWDs (2.8–5.1) for the three samples indicate minor excess data scatter. The SM amphibolite sample, which also yielded U-Pb zircon data, yields an age of 351.8 ± 4.4 Ma (Table 1; Fig. 6a). Apatite from the OR amphibolite sample, which also yielded zircon, yields a U-Pb age of 346.7 ± 5.9 Ma (Table 1; Fig. 6b), while the RW biotite-bearing paragneiss sample from close to the contact with the main Tatra granite yields a U-Pb age of 342.6 ± 7.1 Ma (Table 1; Fig. 6c). The oldest apatites from the AMB-2 amphibolite sample (composed of all grains from trace element population Ap1) yield an unanchored Tera-Wasserburg lower intercept age of 340 ± 31 Ma (Fig. 7a). A small apatite subpopulation (comprised only of grains from trace element population Ap2) yields a mean ^{207}Pb corrected U-Pb age of 328 ± 22 Ma (Fig. 7b), while the youngest apatites from the same sample yield an unanchored Tera-Wasserburg lower intercept age of 259.9 ± 8.3 Ma (Table 1; Fig. 7c). The neighbouring AMB-1 amphibolite sample yields a spread in apatite U-Pb (^{207}Pb corrected) ages from 302 Ma to 135 Ma (Fig. 7d; Table 1).

4.4. Titanite trace element systematics and U-Pb geochronology

Abundant titanite was found in one amphibolite sample from the southern metamorphic envelope (sample AMB-2; Fig. 1c). The titanite forms idiomorphic to sub-idiomorphic crystals from 50 to 150 µm in length, and are elongated within the main lineation and foliation (L-S fabric) of the amphibolite. This evidence for *syn*-tectonic growth (Fig. 2a) combined with the low Al and F contents (Supplementary Table 8) excludes a hydrothermal origin for the titanite in the studied sample (Harlov et al., 2006; Lucassen et al., 2010). It is associated with the main HT-LP metamorphic stage in the Tatra basement (Moussallam et al., 2012) and was contemporaneous with shear-related deformation.

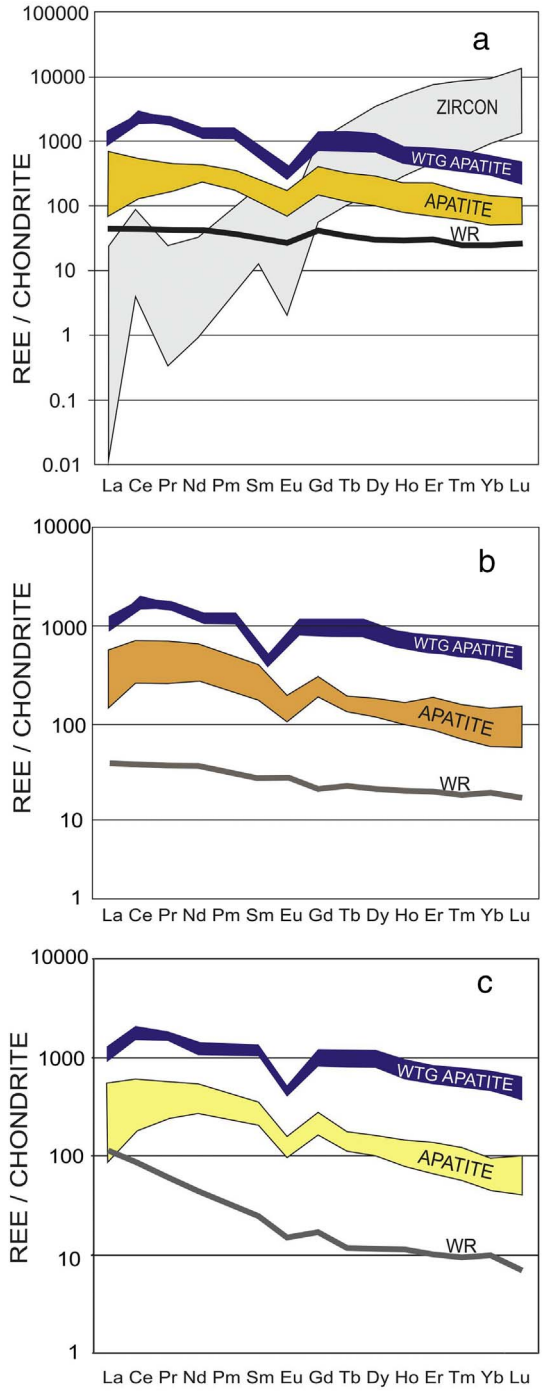

Fig. 4. Chondrite (C1)-normalized (Sun and McDonough, 1995) REE concentrations in accessory minerals and host rocks (amphibolite and gneiss samples) from the northern part of the metamorphic envelope to the Tatra Granite. a. SM amphibolite, b. OR amphibolite; c. RW gneiss.

The total REE content in the titanite crystals ranges from 148 to 2902 ppm, and the chondrite (C1)-normalized REE patterns range from almost flat to LREE-depleted, with Ce_N/Yb_N ratios ranging from 0.02 to 3.86 and correlating positively with the total REE content ($r^2 = 0.84$; Fig. 8a). Eu anomalies range from flat to slightly positive (Eu/Eu* = 0.94–2.34; mean: 1.1; Supplementary Table 4). Titanite from the amphibolite sample AMB-2, which is devoid of any inclusions of rutile or zircon yields an unanchored LA-ICP-MS U-Pb lower intercept Tera-Wasserburg age of 345.3 ± 4.5 Ma (Fig. 6d, Table 2).

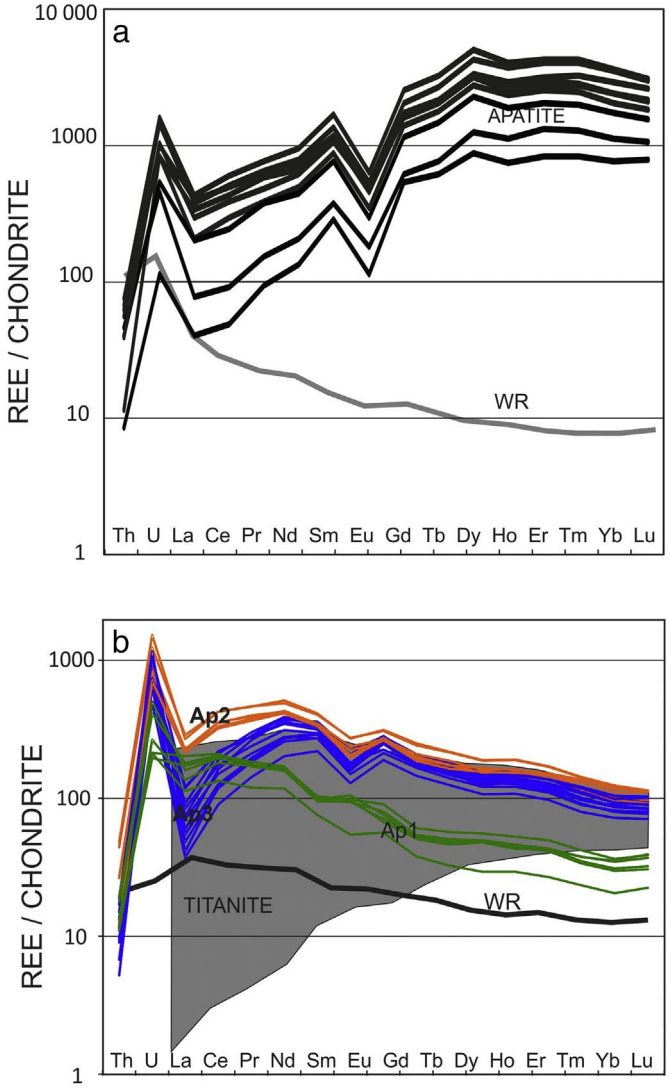

Fig. 5. Chondrite (C1)-normalized (Sun and McDonough, 1995) REE patterns in accessory minerals and host rocks (amphibolite samples) from the southern part of the metamorphic envelope to the Tatra Granite.
a. AMB-1 amphibolite; b. AMB-2 amphibolite.

4.5. Zircon trace element systematics and U-Pb geochronology

Zircon crystals were separated from one amphibolite sample from the northern portion of the metamorphic envelope (sample SM). They are typically 200–300 μm in length, euhedral, differing in aspect ratios of 2:1 to 4:1. The zircons vary from very clear to greenish yellow to reddish brown. The crystals are characterised by a large, extensively metamictized cores with a low CL response, and are surrounded by oscillatory-zoned rims with moderate to weak luminescence (Fig. 9). Seven LA-MC-ICP-MS U-Pb measurements were made on seven zircon crystals. Zircon U-Pb data plot in two groups (Table 3). The first group forming the inner rims (group A), exhibits oscillatory zoning and defines a concordia age of 385 ± 8 Ma (2 sigma; Fig. 10a; Table 3). The second group (group B) comprises the oscillatory-zoned outer rims, and defines a concordia age of 346 ± 6 Ma (2 sigma; Fig. 10b; Table 3).

All analysed zircon crystals ($n = 47$) show HREE-enriched chondrite-normalized patterns (Yb_N/Sm_N = 45–140) with typical positive Ce and strongly negative Eu anomalies (Ce/Ce* = 1.8–295.4; Eu/Eu* = 0.03–0.51; Fig. 4a; Supplementary Table 2). Total REE contents range from 327 to 4318 ppm and Y contents range from 451 to 100 ppm (Supplementary Table 2).

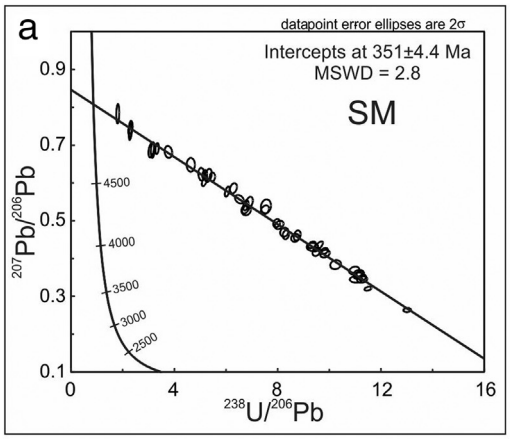

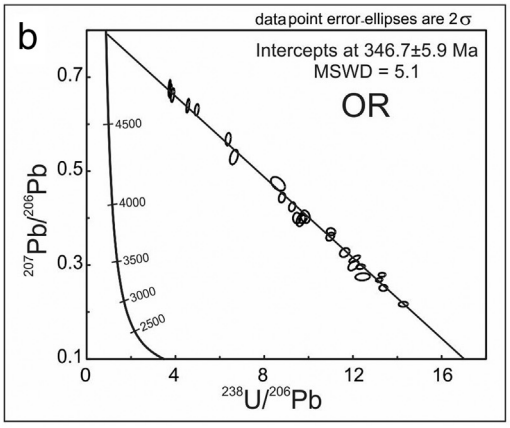

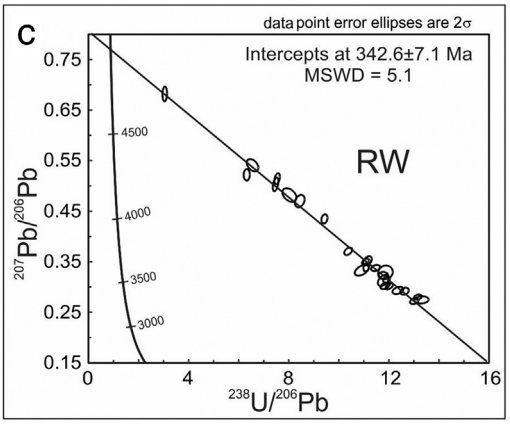

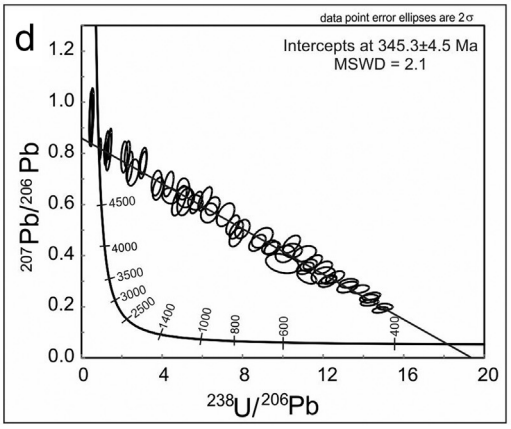

Fig. 6. Tera-Wasserburg concordia diagrams for apatite from the SM, OR, RW samples (northern metamorphic envelope) and Tera-Wasserburg concordia diagram anchored through common Pb for titanite from the AMB-2 sample (southern metamorphic envelope, Western Tatra Mountains).

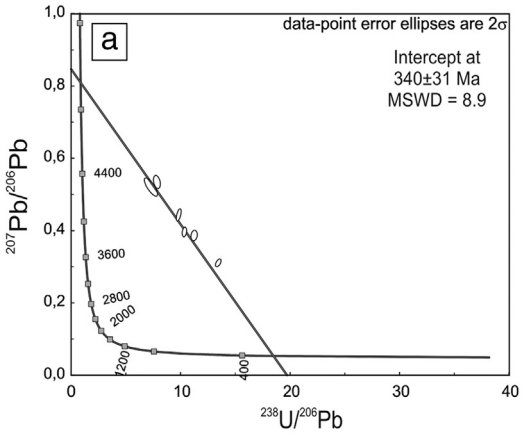

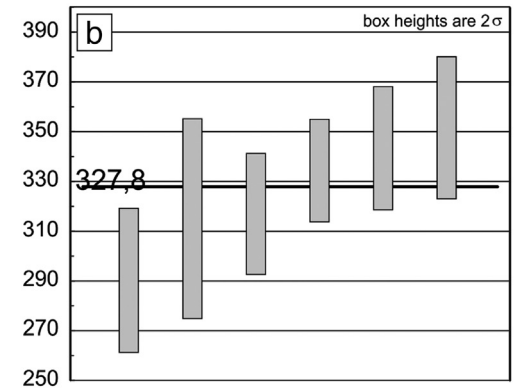

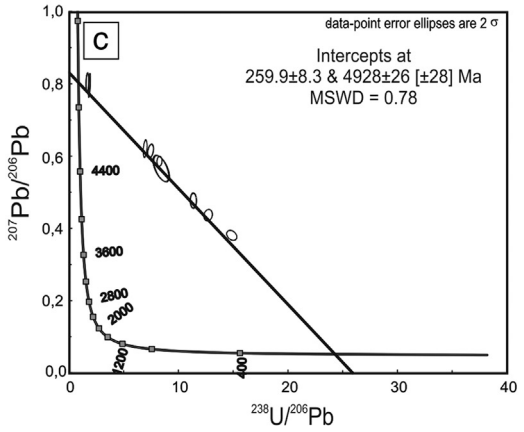

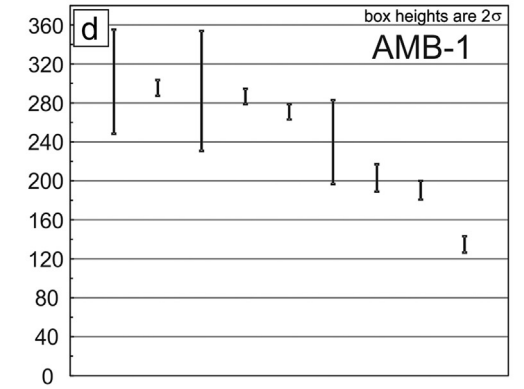

Fig. 7. Tera-Wasserburg concordia diagrams and weighted average ^{207}Pb-corrected U-Pb ages for apatite subpopulations from the AMB-1 and AMB-2 samples.

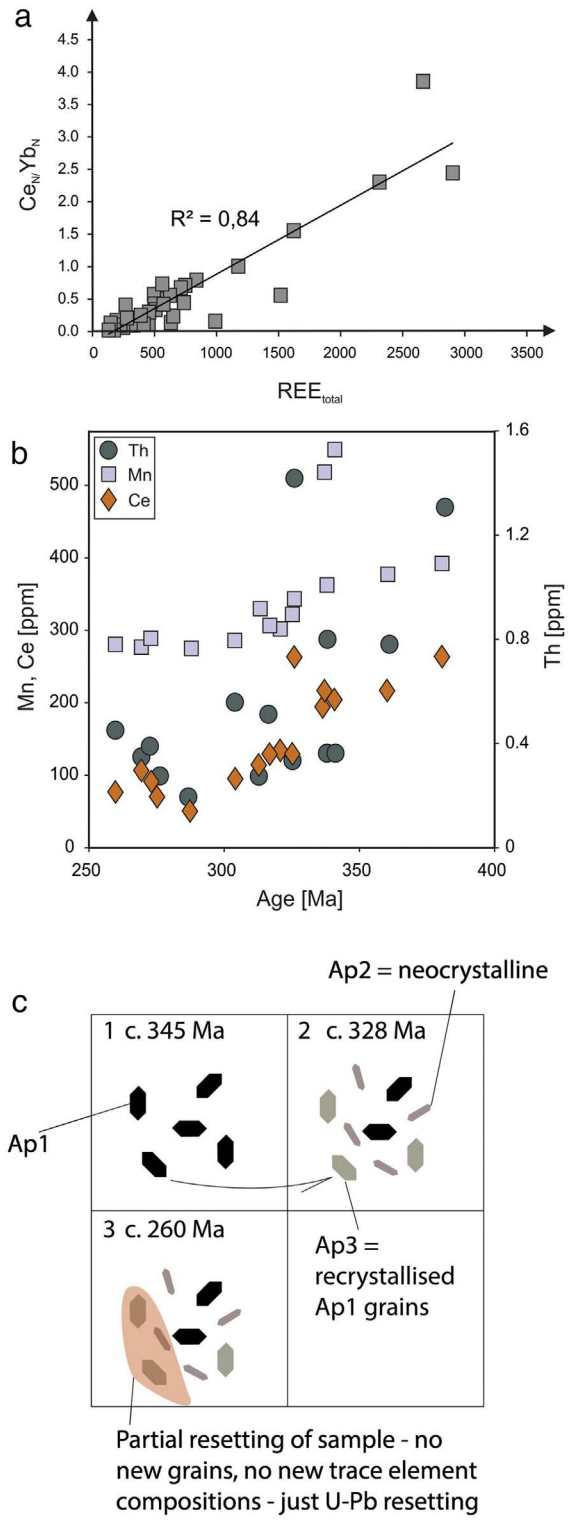

Fig. 8. a) Plot of Ce_N/Yb_N versus total REE content in titanite from sample AMB-2. b) Trace element (Mn, Ce, Th) versus age [Ma] plot for apatite from the AMB-2 sample. c) Illustrative sketch of the paragenesis of apatite Ap1, Ap2 and Ap3 from sample AMB-2.

5. Discussion

The REE patterns in metamorphic rocks are a function of the protolith composition, P-T conditions of metamorphism, composition and activity of metasomatic fluids. The zircon rims overgrowing the metamict zircon cores are interpreted to have grown during partial melting events, a feature characteristic of migmatized metamorphic terranes (Rubatto, 2017 and references therein). The growth of the new zircon rims from the anatectic melt took place during cooling when Zr solubility decreased in the melt and the solidus was reached (Kohn et al., 2015; Rubatto, 2017 and references therein). The REE composition of zircon yields further information on zircon crystallization, particularly regarding the growth of coexisting phases. The REE profiles of the two rim domains do not differ significantly from each other (Fig. 4a), and as the zircon rims crystallized from anatectic melt, the zircon REE compositions are interpreted as being primary magmatic in origin. The strong predominance of HREE over LREE in zircon results from the decreasing ionic radii of REE, making HREE substitution easier in the zircon lattice (Hinton and Upton, 1991; Rubatto, 2002 and references therein). Positive Ce anomalies are typical of all analysed zircon crystals (Supplementary Table 2; Fig. 4a), and result from the incorporation of oxidised Ce^{4+} into the zircon lattice which it preferentially favours over the other LREE, and implies oxidizing conditions during magmatic zircon crystallization. The negative Eu anomalies imply the simultaneous growth of feldspar, incorporating Eu^{2+}, a typical product of the partial melting process.

The other analysed accessory minerals in these rocks (apatite and titanite) either do not behave as passive capsules during metamorphism with regards to the REEs, or re/neocrystallised, and thereby likely record metamorphic processes.

5.1. Metamorphic titanite formation and rare element substitution in titanite

In the studied sample (AMB-2) titanite is a metamorphic mineral which crystallized at the expense of rutile (Fig. 2d). The suggested metamorphic reaction: 2 zoisite + rutile + quartz = 3 anortite + titanite + H_2O (Fig. 2b,d; Kapp et al., 2009) is compatible with the phase relationships determined from petrography and supports the previously suggested P-T path of metamorphism for that part of the Tatra Mountains during decompression and heating from the granite intrusion (Pyka et al., 2014). As an Eu-anomaly is almost absent in the analysed titanites, it is considered unlikely that Eu was fractionated by reduction to Eu^{2+} during this reaction.

The variability of REE fractionation in titanite results from variation in LREE content, as the HREE-contents do not vary between samples (Fig. 5b; Supplementary Table 4). This variability could be interpreted as an effect of changes in LREE content of the metamorphic fluid, low LREE contents in the minerals (e.g. rutile) that titanite crystallized from, or the incorporation of the LREE by the other co-precipitating phases (e.g. apatite, remnant zoisite/allanite; Fig. 2b).

5.2. Rare earth element substitution in apatite

Apatite is the important REE and Y carrier in this metamorphic sample suite (Figs. 4a–c, 5a,b) and is present in every studied rock-type. In metamorphic systems the composition of apatite is a function of temperature, pressure and halogen (HCl, HF) activity in the fluid (Harlov and Förster, 2000, 2002). Assuming no external REE transfer to the metamorphic system, two coupled reactions are believed to govern the REE and Y substitution (Harlov and Förster, 2000):

(1) $(Y + REE)^{3+} + Na^{+} \leftrightarrow 2Ca^{2+}$
(2) $(Y + REE)^{3+} + SiO_4^{4-} \leftrightarrow Ca^{2+} + PO_4^{3-}$

The chondrite-normalized Ce_N/Yb_N ratio is a measure of the depletion or enrichment of the LREE relative to the HREE. Most apatites analysed in this study are enriched in the LREE over the HREE (i.e. they have negative chondrite-normalized REE-slopes; Supplementary Table 9; Figs. 4a–c, 5a,b). A negative Eu anomaly (Eu/Eu*) is observed in all analysed apatite crystals and likely reflects reduction of Eu^{3+} to Eu^{2+}, which is more easily accommodated in the feldspar lattice; as a result Eu is depleted in coexisting apatite. In magmatic and metamorphic systems the oxidation of Ce^{3+} to Ce^{4+} (Bau, 1991 and

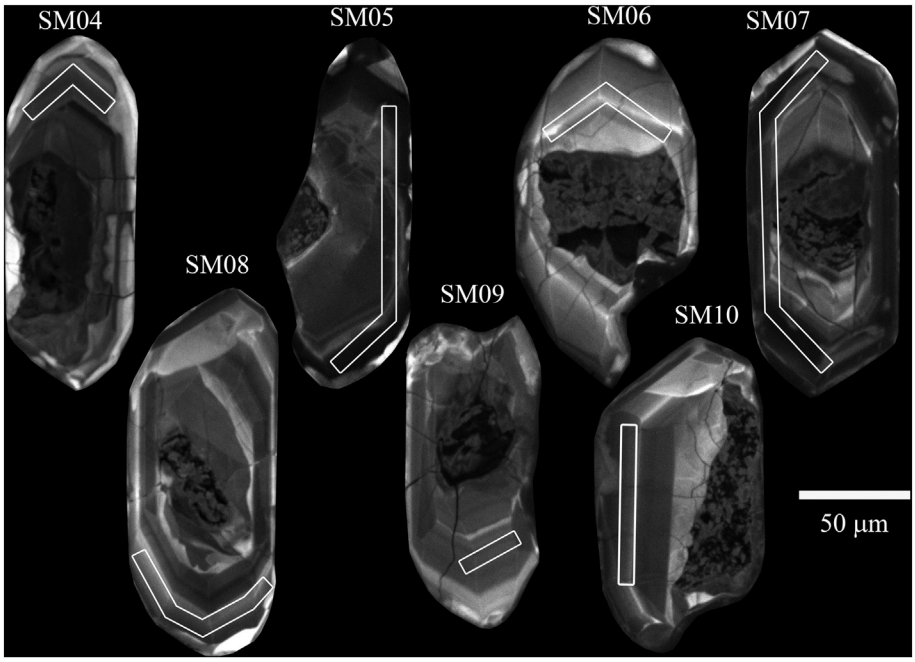

Fig. 9. Cathodoluminescence (CL) images of zircon crystals from the SM sample (Smreczyński Wierch, Western Tatra Mountains).

references therein), gives rise to a slight positive Ce anomaly, which is observed in most of the apatite crystals. The highest Ce anomaly (mean value of 1.17, Supplementary Table 3) is observed in the apatite from the gneiss sample from close to the contact with common Tatra granite. In this sample, apatite is the predominant REE-bearing accessory mineral and hence likely controls the REE budget. While the apatite REE patterns in this gneiss sample have a similar topology to apatite REE spectra from the Western Tatra granite (WTG; Figs. 4a–c), they are an order of magnitude lower.

Apatite crystals in amphibolites from the southern envelope to the Tatra granite differ from the relatively uniform compositions seen in the northern envelope samples. In the amphibolite sample AMB-2, there are three clear populations of apatite, recognized on the basis of different Y, Mn, actinide and REE patterns (Section 4.3; Figs. 5b and 8b). Population Ap1 is interpreted as a metamorphic apatite population with REE patterns almost identical to apatite from the other amphibolite samples and the biotite paragneiss sample from the northern metamorphic envelope (cf. Fig. 5b and Gawęda et al., 2014), and hence these grains are interpreted to have formed under similar metamorphic conditions. Ap2, with the lowest Y contents and highest Ce_N/Yb_N ratios (Fig. 6b; Supplementary Table 3), possibly represents crystallization from a hydrothermal fluid. These Ap2 signatures are consistent with the geochemical characteristics of hydrothermal apatite hosted in plutonic and volcanic rocks from the literature (e.g. Bau and Dulski, 1995; Mao et al., 2016; Migdisov et al., 2016), as well as from the Tatra granitoid intrusion (Szopa, 2009). Contrary to Ap2 apatite, population Ap3 is chemically much more similar to Ap1 apatite, though differs in several key ways. These Ap3 grains have lower LREE, Th and Mn contents, and higher Sr-contents than Ap1 apatite, resulting in high Sm/La ratios (1.54–7.08; Supplementary Table 3; Fig. 5b). As these grains have younger U-Pb ages than Ap1 apatites (Figs. 8a–c), this may indicate that these are grains of Ap1 that recrystallized during later events, becoming depleted in mobile elements such as the LREE in the process (Fig. 8c).

Sample AMB-1, also from the southern envelope, has higher MREE and HREE contents than apatite from any of the other analysed samples, with values similar to Western Tatra Granite (WTG) apatite; this also reflects the whole-rock HREE contents for this sample, which are higher than all other samples (Supplementary Table 3; Fig. 5a). However, unlike WTG apatite, the slope of the AMB-1 apatite REE profile is strongly positive. This may imply apatite growth cogenetic with LREE-hosting phases such as epidote/clinozoisite or monazite.

5.3. Regional implications

Zircon has a closure temperature of at least 900 °C (Lee et al., 1997) for the U-Pb isotopic system, and as such, it can be used to date high-grade metamorphic events. Hoskin and Black (2000) distinguished four types of metamorphic processes which generate metamorphic zircon: 1) precipitation from an anatectic melt formed during partial melting of the host rocks; 2) sub-solidus blastogenesis by Zr and Si diffusion released during breakdown of silicates; 3) precipitation from an aqueous metamorphic fluid; 4) recrystallization of protolith zircon. Inherited zircon cores within the SM sample are metamict (Fig. 9) and could not be dated, while two phases of rim growth were dated. The oscillatory zonation in the inner portions of the rims dated at 385 ± 8 Ma (Fig. 10a) suggests crystallization from melt, and is similar in age to zircon rims from orthogneisses from the same area and dated at 387 ± 14 Ma (Burda and Klötzli, 2011) and 387 ± 8 Ma found in the internal rims of the zircon crystals from OR sample (Gawęda et al., 2016b). This episode of anatexis at c. 387 Ma is likely related to the metamorphic climax at c. 380 to 370 Ma, in the Sowie Mountains in Southern Poland (Timmermann et al., 2000), Śnieżnik Massif in Sudety Mountains (Anczkiewicz et al., 2007) and the Mariánské Lázně Complex in the Czech Republic (Timmerman et al., 2004), and is interpreted as a phase of partial melting during early Variscan orogenesis (Kryza and Fanning, 2007).

The outer portion of the SM zircon rims show similar oscillatory zonation (Fig. 9), which again implies crystallization from melt. These rims, recording partial melting, are dated by the U-Pb zircon method at 346 ± 6 Ma (Fig. 10b; Table 3), and are likely linked to partial melting and migmatization of the metamorphic rocks, including the amphibolites. These ages overlap with an age of 342 ± 9 Ma from zircon (outer)-rims in the OR amphibolite (Gawęda et al., 2016b) and of c. 345 Ma associated with a regional pulse of granitoid magmatism, which is attributed to slab break-off and the input of mantle-derived magma which caused intensive re-heating of the host-rocks, including the more refractory amphibolites (Gawęda et al., 2016a). Partial melting at c. 345 Ma was probably very intensive and associated with fluid

Table 3
LA-MC-ICP-MS U–Pb zircon data from amphibolites of Smreczyński Wierch (SM), Western Tatra Mountains.

Spot #	Blank corrected intensities						Final corrected atomic ratios																					
	^{204}Pb	^{206}Pb	^{207}Pb	^{208}Pb	^{232}Th	^{238}U	^{206}Pb	± 2SE	^{207}Pb	± 2SE	^{206}Pb	± 2SE	Rho	^{207}Pb	± 2SE	^{208}Pb	± 2SE	^{232}Th	^{238}U	± 2SE	^{207}Pb	± 2SE	Age	
	(mV)	(mV)	(mV)	(mV)	(mV)	(mV)	^{204}Pb	(%)	^{235}U	(%)	^{238}U	(%)		^{206}Pb	(%)	^{206}Pb	(%)	^{238}U	^{206}Pb	(%)	^{206}Pb	(%)	Ma	
SM_04	2.7E-06	3.8E-03	2.0E-04	8.5E-05	5.0E-03	9.6E-02	1727	1.42	0.408	8.33	0.05484	8.50	0.51	0.0538	0.75	0.076	7.89	0.015	18.23	8.51	0.0538	0.75	346	± 6
SM_05	1.4E-05	5.8E-03	3.1E-04	2.3E-04	1.4E-02	1.5E-01	2720	7.13	0.394	7.47	0.05255	7.79	0.52	0.0545	0.66	0.129	4.11	0.016	19.03	7.79	0.0545	0.66		
SM_07	2.3E-06	4.0E-03	2.1E-04	1.1E-04	6.4E-03	9.8E-02	3104	1.87	0.417	3.98	0.05584	4.13	0.52	0.0538	0.35	0.070	10.49	0.014	17.91	4.13	0.0538	0.35		
SM_10	3.0E-06	3.1E-03	1.7E-04	1.5E-04	9.2E-03	8.2E-02	2061	0.70	0.408	2.76	0.05411	2.78	0.50	0.05475	0.94	0.181	7.03	0.015	18.48	2.78	0.05475	0.94		
SM_06	2.9E-06	1.8E-03	1.0E-04	5.7E-05	2.8E-03	5.0E-02	2757	0.90	0.459	5.33	0.06119	5.29	0.50	0.05474	0.95	0.107	7.11	0.019	16.34	5.29	0.05474	0.95	385	± 8
SM_08	2.6E-06	2.2E-03	1.1E-04	9.7E-05	5.8E-03	5.5E-02	1369	1.96	0.460	4.17	0.06163	4.15	0.50	0.05418	0.45	0.144	2.35	0.018	16.22	4.15	0.05418	0.45		
SM_09	2.6E-06	2.0E-03	1.1E-04	4.7E-05	2.6E-03	4.7E-02	1318	0.91	0.464	5.78	0.06222	5.78	0.50	0.05412	0.42	0.084	2.60	0.017	16.07	5.78	0.05412	0.42		

mobilization (Gawęda, 1995; Gawęda et al., 2016a).

The U-Pb titanite age from the amphibolite sample AMB-2 at 345.3 ± 4.5 Ma (Fig. 6d, Table 2) is identical (within age uncertainty) to the U-Pb zircon age obtained on the outermost zircon rims.

Similar ages were obtained from U-Pb dating of apatite from all samples from the northern part of the metamorphic envelope (Table 1, Fig. 6a–c). These data are in agreement with Rb-Sr whole-rock dates of c. 345 Ma (Gawęda, 1995) and K-Ar muscovite dates of c. 343 Ma (Deditius, 2004) for pegmatites from the Western Tatra Mountains. The closure temperature for U-Pb apatite system is significantly lower (500–375 °C) than the U-Pb zircon and titanite systems, and the ages broadly overlap with the K-Ar muscovite and whole rock Rb-Sr dates. The simplest explanation is that immediately following the final stages of anatexis recorded by the outermost zircon rims at 346 ± 6 Ma, rapid cooling linked to rapid uplift of the whole metamorphic complex was initiated at c. 345 Ma as recorded by the U-Pb titanite and apatite data and previously published K-Ar muscovite dates. These data are in agreement with the model of Franke (2014) for the Variscan orogeny in Europe, which assumed melting of the crust in a HT/LP regime at c. 340 Ma as a result of rapid uplift. Similar models have been proposed for the Caledonian orogen in Scotland (Baxter et al., 2002), for the Sikkim Himalaya Belt (Anczkiewicz et al., 2014) and for the Greater Himalaya Belt (Grujic et al., 2011). Our data suggest that rapid exhumation was followed by rapid cooling. We propose that the extensional shearing episode provided conduits for melt/fluid flow, which in turn facilitated further extension by softening the crust and enabling rapid heat loss. This could be a general feature in many orogenic belts (see the discussion in Teyssier, 2011).

Both the published U-Pb zircon dating and thermal modelling (Gawęda et al., 2016a) and our U-Pb zircon data do not preclude "hot" conditions (> 700 °C) predominating in the upper continental crust for the time period 385 to 340 Ma. However, the youngest (c. 340 Ma) magmatic episode is only expressed in the eastern part of the Tatra massif (High Tatra Mountains), while in the Western Tatra Mountains the final thermal pulse occurred at c. 345 Ma. As the presented zircon, titanite and apatite ages from northern Tatra metamorphic envelope rocks record an interval of c. 350–345 Ma, we assume a c. 5 Myr interval for cooling from approximately 700 °C (from the geothermometry estimates) to 350 °C (the lowermost closure temperature threshold for the apatite U-Pb system). This implies a c. 70°/Myr cooling rate during rapid uplift of the Tatra block, with an associated change in pressure from 900 to 750 MPa to 520–350 MPa (Gawęda and Włodyka, 2013) which corresponds to an exhumation rate of c. 2 mm/y. The titanite closure temperature is estimated at 633 °C based on the calculated cooling rate, a mean grain radius of 75 μm and the Pb diffusion data of Cherniak (1993, 2010), which is in agreement with the Scott and St-Onge (1995) estimate for Pb diffusion in titanite (660–700 °C). The cooling rate obtained in this study is twice as high as that suggested previously (e.g. Moussallam et al., 2012) and comparable with recent exhumation data from the Moldanubian Unit (Dörr and Zulauf, 2010).

Data from accessory apatite and zircon in the northern part of the metamorphic envelope, as well as titanite from sample AMB-2 in the southern metamorphic envelope (Fig. 6a–d), agree well with the proposed tectono-thermal history characterised by rapid post-Variscan (ca. 345–340 Ma) cooling and uplift. Apatite from amphibolites from the southern metamorphic envelope (the oldest age-population in sample AMB-2) gives a relatively imprecise age of 340 ± 31 Ma (Fig. 7a) and is comprised of grains with similar trace element compositions to apatite in the northern amphibolite samples (e.g. SM, RW, OR; Supplementary Table 3). This implies that these metamorphic apatite grains crystallized under similar metamorphic conditions and at the same time as their northern counterparts (EL Korh et al., 2009; Supplementary Table 3; Fig. 7b). However, a second U-Pb age plateau of c. 328 Ma by dating only population Ap2 apatites (Ap2; Fig. 8b) is interpreted as neocrystalline matrix apatite (Fig. 8c) that formed during a

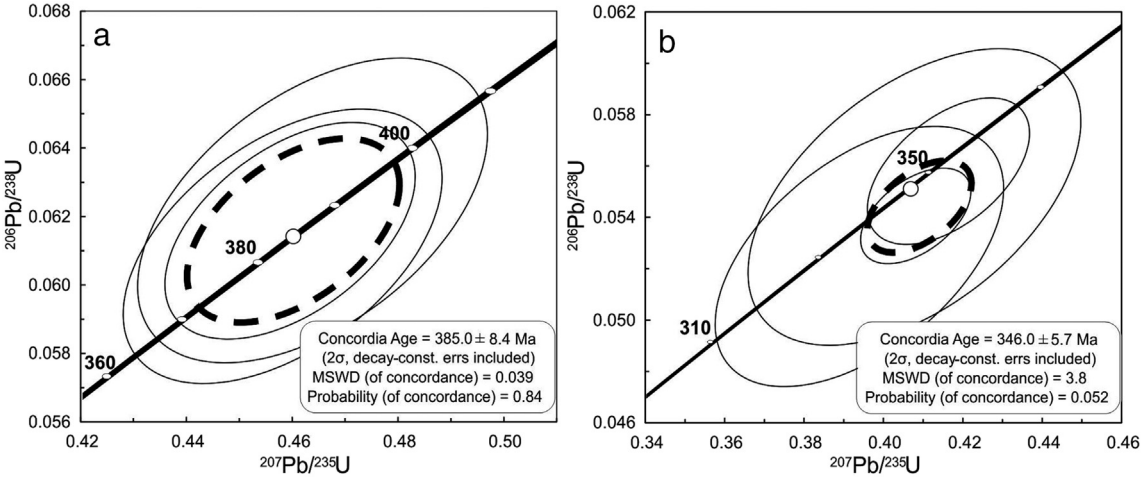

Fig. 10. Concordia plots of LA-MC-ICP-MS zircon analytical results from two age populations in the SM amphibolite sample, Western Tatra Mountains.

later thermal event. This is supported by late-Variscan hydrothermal processes involving (P, F, Ca, REE)-rich fluid migration which have recently been documented in the southern part of the metamorphic envelope and dated at 328 Ma (Gawęda et al., 2016c) and elsewhere in the crystalline cores of the Central Western Carpathians (Burda and Dzierżanowski, 2005; Ondrejka et al., 2012).

Lastly, the youngest age-population in sample AMB-2, is comprised of grains with Ap2 and Ap3 trace element characteristics (Supplementary Table 3; Fig. 5b), and yields a U-Pb age of 260 ± 8 Ma (Fig. 7c). The lack of coupling between this youngest age-population and the trace element data in sample AMB-2 suggests that this poly-metamorphic rock was affected by a final low-temperature event during the Permian. This event must have been hot enough to partially reset the apatite U-Pb system (c. 375 °C), but was not hot enough to induce recrystallization of earlier-formed apatite or to reset the U-Pb system in most grains (Fig. 8c).

The apatite age at c. 260 Ma in sample AMB-2 suggests that these grains are derived from a Permian tectonic event which has been documented by chemical monazite dating in Gemericum (263–276 Ma), Veporicum (Nizke Tatry and Slovenske Rudohorie: 269 ± 22 Ma and 263–269 Ma) as well as in Tatricum (Tríbeč Massif - 273 ± 17 Ma; Finger et al., 2003; Western Tatra Mountains - 258 ± 15 Ma; Burda and Dzierżanowski, 2005). These events are related to granitoid magmatism, at least partly of fluorine-rich A-type affinity (Bonin, 2007), which are associated with extensional tectonics and a high mantle heat flux (Broska and Uher, 2001; Finger et al., 2003 and references therein). These younger apatite U-Pb ages (at c. 328 Ma and 260 Ma) imply the southern metamorphic envelope experienced a more complicated subsequent thermal history, characterised by prolonged cooling and hydrothermal fluid influx.

Apatite crystals from sample AMB-1 yielded U-Pb ages from 302 Ma to 135 Ma (Fig. 8d). The age-spread in apatite from sample AMB-1 suggests that the apatite in this sample either formed, or was fully age-reset, during the late Variscan extensional episode; this apatite would then have subsequently been partially-reset by thermal activity in the early Cretaceous. In Veporicum and Gemericum (Fig. 1b) the Cimmerian orogeny (associated with the closure of the Meliata Ocean and obduction of the accretionary prism) resulted in nappe stacking dated at ~135–95 Ma, which caused a burial of the crystalline basement of the Veporic Unit to depths of ~15–40 km with an associated greenschist- to amphibolite-facies metamorphic overprint (Vojtko et al., 2016). The youngest apatite U-Pb ages found in the AMB-1 sample could most simply be explained by variable age-resetting associated with thermal activity related to this Cimmerian event.

The post-Variscan histories of the southern and northern parts of the metamorphic envelope are very different. The northern portion exhibits no significant thermal activity since the Variscan, and the southern portion experiencing a more complicated subsequent history with Permian to Cretaceous overprinting of the Variscan exhumation and cooling history. In light of this, we speculate that before rotation in the Neogene (Csontos and Vörös, 2004) the southern metamorphic envelope to the Tatra Mountains shared a common geological development with Veporicum and/or Gemericum, in contrast to the northern metamorphic envelope, which was shaped only by Variscan orogenic events.

6. Conclusions

Cooling and uplift of the Western Tatra crystalline basement took place in the final stages of the Variscan orogeny. Apatite from the northern metamorphic envelope preserves U-Pb cooling ages of ca. 345 Ma, consistent with U-Pb titanite and zircon ages from the same rocks. The large differences in the U-Pb temperature sensitivity of the analysed phases implies therefore very rapid cooling. The climax of peak metamorphism followed by immediate onset of simultaneous late Variscan exhumation of the whole Western Tatra Mountains block took place at c. 345 Ma as supported by zircon, titanite and apatite U-Pb ages, and is recorded mainly in the northern part of the metamorphic cover.

In contrast, apatite crystals from the southern metamorphic envelope experienced also late Variscan (P, F, Ca, REE)-rich hydrothermal fluid circulation and Permian to Cretaceous overprinting of the Variscan exhumation and cooling history. Late c. 260 Ma resetting in the southern metamorphic envelope was possibly related to the emplacement of Permian A-type granites. Mesozoic apatite U-Pb ages found in one amphibolite sample from the southern metamorphic envelope can be explained by variable age-resetting associated with thermal activity related to a Mesozoic (Cimmerian) event.

Supplementary data to this article can be found online at https://doi.org/10.1016/j.chemgeo.2018.03.012.

Acknowledgements

We thank Mrs Lidia Jeżak for her help during microprobe analyses. Comments of the handling editor Klaus Mezger, co-editor K. Sajeev, reviewers Vinod O. Samuel and M. Guitreau and one anonymous reviewer led to clearer presentation of the paper and are deeply acknowledged. The whole study was financially supported by the Polish National Science Centre (NCN) grant No. 2012/07/B/ST10/04366 (given to AG) and Science Foundation Ireland grant 12/IP/1663 (awarded to DC).

References

Aleinikoff, J.N., Wintsch, R.P., Fanning, C.M., Dorais, M.J., 2002. U–Pb geochronology of zircon and polygenetic titanite from the Glastonbury complex, Connecticut, USA: an integrated SEM, EMPA, TIMS, and SHRIMP study. Chem. Geol. 188, 125 – 147.

Anczkiewicz, R., Szczepański, J., Mazur, S., Storey, C., Crowley, Q., Vill, I.M., Thirlwall, M.F., Jeffries, T.E., 2007. Lu-Hf geochronology and trace element distribution in garnet: implications for uplift and exhumation of ultra-high pressure granulites in the Sudetes, SW Poland. Lithos 95, 363–380.

Anczkiewicz, R., Chakraborty, S., Dasgupta, S., Mukhopadhyay, D., Kołtronik, K., 2014. Timing, duration and inversion of prograde Barrovian metamorphism constrained by high resolution Lu-Hf garnet dating: a case study from the Sikkim Himalaya, NE India. Earth Planet. Sc. Lett. 407, 70–81.

Bau, M., 1991. Rare-earth element mobility during hydrothermal and metamorphic fluid-rock interaction and the significance of the oxidation state of europium. Chem. Geol. 93, 219–230.

Bau, M., Dulski, P., 1995. Comparative study of yttrium and rare-earth element behaviours in flourine-rich hydrothermal fluids. Contrib. Mineral. Petrol. 119, 213–223.

Baxter, E.E., Ague, J.J., Depaolo, D.J., 2002. Prograde temperature-time evolution in the Barrovian type-locality constrained by Sm/Nd garnet age from Glen Clova, Scottland. J. Geol. Soc. 159, 71–82.

Blundy, J.D., Holland, T.J.B., 1990. Calcic amphibole equilibria and a new amphibole-plagioclase geothermometer. Contrib. Mineral. Petrol. 104, 208–244.

Bonin, B., 2007. A-type granites and related rocks: evolution of a concept, problems and prospects. Lithos 97, 1–29.

Broska, I., Uher, P., 2001. Whole-rock chemistry and genetic typology of West Carpathians Variscan granitoids. Geol. Carpath. 52, 79–90.

Buick, I.S., Maas, R., Gibson, R., 2001. Precise U-Pb titanite age constraints on the emplacement of the Bushweld Complex, South Africa. J. Geol. Soc. 158, 3–6. http://dx.doi.org/10.1144/jgs.158.1.3.

Burda, J., Dzierżanowski, P., 2005. Electron microprobe dating of monazite from migmatitic gneiss from the Western Tatra Mts. Mineralogical Society of Poland. Spec. Pap. 25, 277–280.

Burda, J., Gawęda, A., 2009. Shear-influenced partial melting in the Western Tatra metamorphic complex: geochemistry and geochronology. Lithos 110, 373–385.

Burda, J., Klötzli, U., 2011. Pre-Variscan evolution of the Western Tatra Mountains: new insights from U-Pb zircon dating. Mineral. Petrol. 102, 99–115. http://dx.doi.org/10.1007/s00710-011-0176-4.

Burda, J., Gawęda, A., Golonka, J., Majka, J., Wiedenbeck, M., Pyka, P., 2015. Rheic Ocean history imprinted in zircon from metabasite: a case of the Western Tatra Mountains, Poland/Slovakia. Mineralogia – Spec. Pap. 44, 30.

Cherniak, D.J., 1993. Led diffusion in titanite and preliminary results on the effects of radiation damage on Pb transport. Chem. Geol. 110, 177–194.

Cherniak, D.J., 2010. Diffusion in accessory minerals: zircon, titanite, apatite, monazite and xenotime. Rev. Mineral. Geochem. 72, 827–869. http://dx.doi.org/10.2138/rmg.2010.72.18.

Chew, D.M., Donelick, R.A., 2012. Combined apatite fission track and U-Pb dating by LA-ICPMS and future trends in apatite provenance analysis. In: Sylvester, P. (Ed.), Quantitative Mineralogy and Microanalysis of Sediments and Sedimentary Rocks. Mineral. Assoc., Canada, pp. 219–248.

Chew, D.M., Spikings, R.A., 2015. Geochronology and thermochronology using apatite: time and temperature lower crust to surface. Elements 11, 189–194. http://dx.doi.org/10.2113/gselements.11.3.189.

Chew, D.M., Sylvester, P.J., Tubrett, M.N., 2011. U-Pb and Th-Pb dating of apatite by LA-ICP-MS. Chem. Geol. 280, 200–216. http://dx.doi.org/10.1016/j.chemgeo.2010.11.010.

Chew, D.M., Petrus, J.A., Kamber, B.S., 2014. U-Pb LA-ICPMS dating using accessory mineral standards with variable common Pb. Chem. Geol. 363, 185–199.

Chew, D., Babechuk, M.G., Cogne, M., Mark, C., O'Sullivan, G.J., Henrichs, I.A., Doepke, D., McKenna, C.A., 2016. (LA,Q)-ICPMS trace element analyses of Durango and McClure Mountain apatite and implications for making natural LA-ICPMS mineral standard. Chem. Geol. 435, 35–48.

Cochrane, R., Spikings, R.A., Chew, D., Wotzlaw, J.-F., Chiaradia, M., Tyrrell, S., Schaltegger, U., Van der Lelijl, R., 2014. High temperature (> 350 °C) thermochronology and mechanisms of Pb loss in apatite. Geochim. Cosmochim. Acta 127, 39–56.

Corsini, M., Bosse, V., Feraud, G., Demoux, A., Crevola, G., 2010. Exhumation processes during post-collisional stage in the Variscan belt revealed by detailed $^{40}Ar/^{39}Ar$ study (Tanneron Massif, SE France). Int. J. Earth Sci. 99 (2), 327–341. http://dx.doi.org/10.1007/s00531-008-0397-x.

Csontos, L., Vörös, A., 2004. Mesozoic plate tectonic reconstruction of the Carpathian region. Palaeogeogr. Palaeocl. 210, 1–56.

Deditius, A., 2004. Petrology and Isotopic age of the Muscovite Blasthesis From the Mylonitic Zones in the Crystalline Rocks of the Western Tatra Mountains. Geologia 16. 133–152 University of Silesia publishing House (in Polish with English abstract).

Dörr, W., Zulauf, G., 2010. Elevator tectonics and orogenic collapse of a Tibetan-style plateau in the European Variscides: the role of the bohemian shear zone. Int. J. Earth Sci. 99, 299–325. http://dx.doi.org/10.1007/s00531-008-0389-x.

EL Korh, A., Schmidt, S.Th., Ulianov, A., Potel, S., 2009. Trace element partitioning in HP-LT metamorphic assemblages during subduction-related metamorphism, Ile de Groix, France: a detailed LA-ICPMS study. J. Petrol. 50, 1107–1148. http://dx.doi.org/10.1093/petrology/egp034.

Finger, F., Broska, I., Haunschmid, B., Hrasko, L., Kohut, M., Krenn, E., Petrik, I., Riegler, G., Uher, P., 2003. Electron-microprobe dating of monazites from Western Carpathian basement granitoids:plutonic evidence for an important Permian rifting event subsequent to Variscan crustal anataxis. Int. J. Earth Sci. 92, 86–98. http://dx.doi.org/10.1007/s00531-002-0300-0.

Franke, W., 2014. Topography of the Variscan orogen in Europe: failed–not collapsed. Int. J. Earth Sci. 103, 1471–1499. http://dx.doi.org/10.1007/s00531-014-1014-9.

Gawęda, A., 1995. Geochemistry and Rb/Sr isochron age of pegmatites from the Western Tatra Mts. (S-Poland). Geol. Carpath. 46, 95–99.

Gawęda, A., Burda, J., 2004. Evolution of Metamorphism and Deformation in the Crystalline Complex of the Tatra Mountains. Geologia 16. 153–187 University of Silesia publishing House (in Polish with English abstract).

Gawęda, A., Szopa, K., 2011. The origin of magmatic layering in the high Tatra granite, Central Western Carpathians – implications for the formation of granitoid plutons. Earth Env. Sci. T. Royal Soc. Edinb. 103, 129–144. http://dx.doi.org/10.1017/S1755691012010146.

Gawęda, A., Włodyka, R., 2013. The origin of post-magmatic Ca-Al minerals in granite-diorite mingling zones: the Tatra granitoid intrusion, Western Carpathians. N Jhb. Mineral. Abh. 190 (1), 29–47. http://dx.doi.org/10.1127/0077-7757/2012/0228.

Gawęda, A., Winchester, J.A., Kozłowski, K., Narębski, W., Holland, G., 2000. Geochemistry and paleotectonic setting of the amphibolites from the Western Tatra Mountains. Geol. J. 35, 69–85.

Gawęda, A., Szopa, K., Chew, D., 2014. LA-ICP-MS U-Pb dating and REE patterns of apatite from the Tatra Mountains, Poland as a monitor of the regional tectonomagmatic activity. Geochronometria 41 (4), 306–314. http://dx.doi.org/10.2478/s13386-013-0171-0.

Gawęda, A., Burda, J., Klötzli, U., Golonka, J., Szopa, K., 2016a. Episodic construction of the Tatra granitoid intrusion (Central Western Carpathians, Poland/Slovakia): consequences for the geodynamics of Variscan collision and Rheic Ocean closure. Int. J. Earth Sci. 105, 1153–1174. http://dx.doi.org/10.1007/s00531-015-1239-2.

Gawęda, A., Burda, J., Klötzli, U., Golonka, J., Szopa, K., 2016b. How many ocean floors? Geochemical and geochronological study of amphibolites from the Western Tatra Mountains (Central Western Carpathians). In: Minerals, Rocks and Fluids: Alphabet and Words of Planet Earth — 2nd European Mineralogical Conference Abstract Book, 629.

Gawęda, A., Szopa, K., Chew, D., Klötzli, U., Müller, A., Sikorska, M., Pyka, P., 2016c. Age and origin of fluorapatite-rich dyke from Baranec Mt. (Tatra Mts., Western Carpathians): a key to understanding of the post-orogenic processes and element mobility. Geol. Carpath. 67, 417–432. http://dx.doi.org/10.1515/geoca-2016-0026.

Gawęda, A., Burda, J., Golonka, J., Klötzli, U., Chew, D., Szopa, K., Wiedenbeck, M., 2017. The evolution of Eastern Tornquist-Paleoasian Ocean and subsequent continental collisions: a case study from the Western Tatra Mountains, Central Western Carpathians (Poland). Gondwana Res. 48, 134–152. http://dx.doi.org/10.1016/j.gr.2017.04.021.

Golonka, J., Pietsch, K., Marzec, P., Kasperska, M., Cichostępski, K., Dec, J., Lasocki, S., Mirek, J., Orlecka-Sikora, B., 2016. Central Carpathians — North European plates suture zone in Poland. In: Šujan, M. (Ed.), Environmental, Structural and Stratigraphical Evolution of the Western Carpathians: 10th ESSEWECA Conference. Abstract Book, 1st–2nd December 2016, Bratislava, Slovakia, pp. 31–32.

Grabowski, J., Gawęda, A., 1999. Preliminary paleomagnetic study of the high Tatra granites, Central Western Carpathians. Poland. Geol. Quarterly 43, 263–276.

Grujic, D., Warren, C.J., Wooden, J.L., 2011. Rapid syn-convergent exhumation of Miocene aged lower orogenic crust in the Eastern Himalaya. Lithosphere 3, 346–366. http://dx.doi.org/10.1030/L154.1.

Harlov, D.E., Förster, H.-J., 2000. Unraveling the history of high-grade rocks: what apatite may tell us? J. Czech Geol. Soc. 48, 59–60.

Harlov, D.E., Förster, H.-J., 2002. High-grade fluid metasomatism on both a local and regional scale: the Seward Peninsula, Alaska and the Val Strona di Omegna, Ivrea – Verbano zone, northern Italy. Part II. Phosphate mineral chemistry. J. Petrol. 43, 801–824.

Harlov, D., Tropper, P., Seifert, W., Nijand, T., Förster, H.-J., 2006. Formation of Al-rich titanite ($CaTiSiO_4O$–$CaAlSiO_4OH$) reaction rims on ilmenite in metamorphic rocks as a function of $\int H_2O$ and $\int O_2$. Lithos 88, 72–84. http://dx.doi.org/10.1016/j.lithos.2005.08.005.

Henry, D.J., Guidotti, C.V., Thomson, J.A., 2005. The Ti-saturation surface for low-to-medium pressure metapelitic biotites: implications for geothermometry and Ti substitution mechanism. Am. Mineral. 90, 316–328.

Hinton, R.W., Upton, B.G.W., 1991. The chemistry of zircon: variation within and between large crystals from syenite and alkali basalt xenoliths. Geochim. Cosmochim. Acta 55, 3287–3302.

Hoskin, P.W.O., Black, L.P., 2000. Metamorphic zircon formation by solid-state recrystallization of protolith igneous zircon. J. Metamorph. Geol. 18, 423–439.

Janák, M., O'Brien, P.J., Hurai, V., Reutel, C., 1996. Metamorphic evolution and fluid composition of garnet-clinopyroxene amphibolites from the Tatra Mountains, Western Carpathians. Lithos 39, 57–79.

Kapp, P., Manning, C.E., Tropper, P., 2009. Phase equilibria constraints on titanite and rutile activities in mafic epidote amphibolites and geobarometry using titanite-rutile equilibria. J. Metamorph. Geol. 27, 509–521. http://dx.doi.org/10.1111/j.1525-1314.2009.00836.x.

Kennedy, A.K., Kamo, S.L., Nasdala, L., Timms, N.E., 2010. Grenville skarn titanite: potential reference material for SIMS U-Th-Pb analysis. Can. Mineral. 48, 1423–1443.

Kennedy, A.K., Wotzlaw, J.-F., Schaltegger, U., Crowley, J.L., Schmitz, M., 2014. Eocene zircon reference material for microanalysis of U-Th-Pb isotopes and trace elements. Can. Mineral. 52 (3), 409–421. http://dx.doi.org/10.3749/canmin.52.3.409.

Klötzli, U., Klötzli, E., Günes, Z., Košler, J., 2009. External accuracy of laser ablation U-Pb zircon dating: results from a test using five different reference zircons. Geostand. Geoanal. Res. 33 (1), 5–15.

Kohn, M.J., 2017. Titanite petrochronology. Rev. Mineral. Geochem. 83 (1), 419–441.

Kohn, M.J., Corrie, S.L., Markley, C., 2015. The fall and rise of metamorphic zircon. Am.

Mineral. 100 (4), 897–908. http://dx.doi.org/10.2138/am-2015-5064.
Kohut, M., Janak, M., 1994. Granitoids of the Tatra Mts., Western Carpathians: field relations and petrogenetic implications. Geol. Carpath. 45 (5), 301–311.
Kryza, R., Fanning, C.M., 2007. Devonian deep-crustal processes and uplift in the Variscan Orogen: evidence from SHRIMP zircon ages from the HT-HP granulites and migmatites of the Góry Sowie (Polish Sudetes). Geodin. Acta 20 (3), 159–175.
Lee, J.K.W., Williams, I.S., Ellis, D.J., 1997. Pb, U and Th diffusion in natural zircon. Nature 390, 159–162.
Lucassen, F., Franz, G., Rhede, D., Wirth, R., 2010. Ti-Al zoning of experimentally grown titanite in the system CaO-Al_2O_3-TiO_2-SiO_2-NaCl-H_2O-(F): evidence for small-scale fluid heterogeneity. Am. Mineral. 95, 1365–1378. http://dx.doi.org/10.2138/am.2010.3518.
Ludwig, K.R., 2003. Isoplot/Ex 3.00: A Geochronological Toolkit for Microsoft Excel. Berkeley Geochronology Center Special Publication (4, 70 p).
Mao, M., Alexei, S.R., Stephen, M.R., Jody, S., Laurence, A.C., 2016. Apatite trace element compositions: a robust new tool for mineral exploration. Econ. Geol. 111, 1187–1222.
Migdisov, A.A., Williams-Jones, A.E., Brugger, J., Caporuscio, F.A., 2016. Hydrothermal transport, deposition, and fractionation of the REE: experimental data and thermodynamic calculations. Chem. Geol. 439, 13–42. http://dx.doi.org/10.1016/j.chemgeo.2016.06.005.
Möller, A., Mezger, K., Shenk, K., 2000. U–Pb dating of metamorphic minerals: Pan-African metamorphism and prolonged slow cooling of high pressure granulites in Tanzania, East Africa. Precambrian Res. 104 (3–4), 123–146.
Moussallam, Y., Schneider, D.A., Janak, M., Thoni, M., Holm, D.K., 2012. Hetereogeneous extrusion and exhumation of deep-crustal Variscan assembly: geochronology of the Western Tatra Mountains, northern Slovakia. Lithos 144-145, 88-10. http://dx.doi.org/10.1016/j.lithos.2012.03.025.
Ondrejka, M., Uher, P., Putiš, M., Broska, I., Bačik, P., Konečny, P., Schmiedt, I., 2012. Two-stage breakdown of monazite by post-magmatic and metamorphic fluids: an example of the Veporic orthogneiss, Western Carpathians, Slovakia. Lithos 142–143, 245–255.
Paton, C., Helistrom, J., Paul, B., Woodhead, J., Herqt, J., 2011. Iolite: freeware for the visualisation and processing of mass spectrometric data. J. Anal. Atom. Spectrom. 26, 2508–2518. http://dx.doi.org/10.1039/C1JA10172B.
Petrik, I., Broska, I., Uher, P., 1994. Evolution of the Western Carpathian granite magmatism: age, source rocks, geotectonic setting and relation to the Variscan structure. Geol. Carpath. 45, 283–291.
Petrus, J.A., Kamber, B.S., 2012. VizualAge: a novel approach to laser ablation ICP-MS U-Pb geochronology data reduction. Geostand. Geoanal. Res. 36 (3), 247–270.
Piotrowska, K., Kotański, Z., Gawęda, A., Piotrowski, J., Rączkowski, W., 2014. Geological Map of Poland – Western Tatra Mountains 1: 50 000. Polish Geological Institute – National Research Institute, Warsaw.
Pyka, P., Gawęda, A., Szopa, K., Müller, A., Sikorska, M., 2014. Petrogenesis of kyanite-quartz segregations in mica schists of the Western Tatra Mountains (Slovakia). Fortschr. Mineral. 45 (3–4), 99–120. http://dx.doi.org/10.1515/mipo-2015-0007.
Roberts, M.P., Finger, F., 1997. Do U-Pb zircon ages from granulites reflect peak metamorphic conditions? Geology 25, 319–322.
Rubatto, D., 2002. Zircon trace element chemistry: partitioning with garnet and the link between the U-Pb ages and metamorphism. Chem. Geol. 184, 123–138.
Rubatto, D., 2017. Zircon: the metamorphic mineral. Rev. Mineral. Geochem. 83 (1), 261–295. http://dx.doi.org/10.2138/rmg.2017.83.09.
Schmidt, M.W., 1992. Amphibole equilibria in tonalite as a function of pressure: an experimental calibration of the Al-in-hornblende barometer. Contrib. Mineral. Petrol. 110, 304–310.
Schmitz, M.D., Bowring, S.A., 2001. U-Pb zircon and titanite systematics of the fish canyon tuff: an assessment of high precision U-Pb geochronology and its application to young volcanic rocks. Geochim. Cosmochim. Acta 65 (15), 2571–2587. http://dx.doi.org/10.1016/S0016-7037(01)00616-0.
Schoene, B., Bowring, S.A., 2006. U-Pb systematics of the McClure Mountain syenite: thermochronological constraints on the age of the Ar-40/Ar-39 standard MMhb. Contrib. Mineral. Petrol. 151 (5), 615–630.
Schoene, B., Bowring, S.A., 2007. Determining accurate temperature-time paths from U-Pb thermochronology: an example from the Kaapval craton, southern Africa. Geochim. Cosmochim. Acta 71 (1), 165–185.
Scott, D.J., St-Onge, M.R., 1995. Constraints on Pb closure temperature in titanite based on rocks from the Ungava Orogen, Canada: implication on U-Pb geochronology and P-T-t path determination. Geology 23 (12), 1123–1126.
Sláma, J., Kostler, J., Condon, D.J., Crowley, J.L., Gerdes, A., Hanchar, J.M., Horstwood, M.S.A., Morris, G.A., Nasdala, B., Turbett, M.N., Whitehouse, M.J., 2008. Plešovice, a new natural reference material for U–Pb and Hf isotopic analysis. Chem. Geol. 249, 1–35.
Śmigielski, M., Sinclair, H.D., Stuart, F.M., Persano, C., Krzywiec, P., 2016. Exhumation history of the Tatry Mountains, Western Carpathians, constrained by low-temperature thermochronology. Tectonics 35, 187–207. http://dx.doi.org/10.1002/2015TC003855.
Stacey, J.S., Kramers, J.D., 1975. Approximation of terrestrial lead isotope evolution by a two-stage model. Earth Planet. Sci. Lett. 26, 207–221.
Sun, S.S., McDonough, W.F., 1995. The composition of the Earth. Chem. Geol. 120, 223–253.
Sylvester, P.J., Ghaderi, M., 1997. Trace elements analysis of scheelite by excimer laser ablation-inductively coupled plasma-mass spectrometry (ELA-ICP-MS) using a synthetic silicate glass standard. Chem. Geol. 141 (1–2), 46–65.
Szopa, K., 2009. The same reaction but different environment: breakdown of monazite in the high Tatra granites. Mineralogia - Special Pap. 35, 113.
Teyssier, C., 2011. Exhumation of deep orogenic crust. Lithosphere 3, 439–443. http://dx.doi.org/10.1030/RF.L002.1.
Timmerman, H., Štědrá, V., Gerdes, A., Noble, S.R., Parrish, R.R., Dörr, W., 2004. The problem of dating high-pressure metamorphism: a U-Pb isotope and geochemical study on eclogites and related rocks of the Mariánske Lázně Complex, Czech Republic. J. Petrol. 45 (7), 1311–1338.
Timmermann, H., Parrish, R.R., Noble, S.R., Kryza, R., 2000. New U-Pb monazite and zircon data from the Sudetes Mountains in SW Poland: evidence for a single-cycle Variscan orogeny. J. Geol. Soc. 157, 265–268. http://dx.doi.org/10.1144/jgs.157.2.265.
Vojtko, R., Králiková, S., Jeřábek, P., Schuster, R., Danišík, M., Fügenschuh, B., Minár, J., Madarás, J., 2016. Geochronological evidence for the Alpine tectono-thermal evolution of the Veporic unit (Western Carpathians, Slovakia). Tectonophysics 666, 48–65.
Wiedenbeck, M., Allé, P., Corfu, F., Griffin, W.F., Meier, M., Oberli, F., von Quadt, A., Roddick, J.C., Spiegel, W., 1995. Three natural zircon standards for U-Th-Pb, Lu-Hf, trace elements and REE analyses. Geostand. Geoanal. Res. 19 (1), 1–23.